Analysis of a versatile moving-belt mechanism for the control of wall-bounded flows

Thomas R. Bewley

Flow Control Lab, Dept. of MAE, UC San Diego, La Jolla, CA 92093, USA

This paper considers a remarkably simple yet versatile moving-belt mechanism for the control of both laminar and turbulent wall-bounded flows. The mechanism considered can be used in both the passive and active setting, and shows potential for a variety of possible aeronautical, maritime, and microfluidic applications, including drag reduction, transition delay, power extraction (e.g., electricity generation), power addition (fluid pumping), detection and prevention of separation/stall, thrust production, lift enhancement, and attitude control. Prospects for the designs considered are especially attractive for small unmanned vehicles and "microfluidic" applications in which viscous effects are dominant and the efficiency of traditional higher-Reynolds number designs is degraded. In the present paper, we first review much of the older literature on the subject of moving-belt and rotating-cylinder strategies for flow control. We then focus on several new analytic results and nondimensional similarity solutions which may be attained with the present mechanism when applied in the laminar setting, including generalizations of the Blasius boundary layer and asymptotic-suction boundary layer profiles. Such results clarify some of the important tradeoffs (with cavity depth, roller size, etc.) involved in extending this control strategy to practical implementations. Several promising future applications of the moving-belt mechanism are also proposed. This article contains 62 references.

1 Introduction

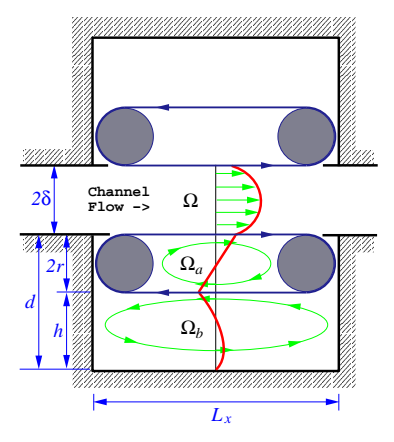


Figure 1: Moving-belt mechanism applied to plane channel flow. The flow profiles within the upper cavity are similar to the profiles shown in the lower cavity. In our initial analysis, the belt is driven to some nonzero velocity u_w passively via the friction imparted by the flow in the channel, and we assume negligible entrainment of the flow from Ω into Ω_b around the ends of the rollers. In later sections, we discuss the consequences of applying the moving-belt mechanism to boundary layer flows, coupling it with suction, allowing for entrainment of the main flow into Ω_b , and attaching an electric generator or motor to the roller supports.

This article considers the moving-belt mechanism illustrated in Figure 1 for the control of wall-bounded flows. At first glance, the effect of this mechanism on the overlying flow is quite simple: it changes the boundary condition on the streamwise component of velocity in Ω from no-slip to some nonzero value, which may in fact be specified if motors are used to drive the rollers to actively control the belt speed. An important issue that has previously been largely overlooked is that, in most practical configurations, the moving-belt mechanism is filled with the same viscous fluid (air, water, ...) as the overlying flow, and thus the losses due to the recirculating fluid within Ω_a and Ω_b are significant. An equilibrium is reached when the drag force imparted on the belt by the flows in Ω , Ω_a , and Ω_b is balanced by the force imparted on the belt by the torques applied at the roller supports and the parasitic effects caused by bearing friction and belt deformation. A primary focus of the present paper is to quantify this hydrodynamic

¹Transmitted by Associate Editor M. Gad-el-Hak

equilibrium in the "best case" (that is, neglecting the losses due to bearing friction and belt deformation) and interpret its implications in terms of the possible suitability of this mechanism for a variety of practical applications.

1.1 Approaches based on the Magnus effect

The idea of using a moving surface to control a wall-bounded flow has its genesis in the Magnus effect, whereby an isolated rotating cylinder in crossflow provides a substantial amount of lift. Magnus [5] observed and explained this phenomenon, thereby "solving" the militarily important problem of the frequent deviation of artillery shells from their theoretical trajectories. This effect eventually became known as the "Magnus effect", though several investigators, both before and after Magnus, contributed to its understanding. For detailed historical accounts of the early experimental and theoretical explorations of this effect, see Swanson [6] and Tokaty [1].

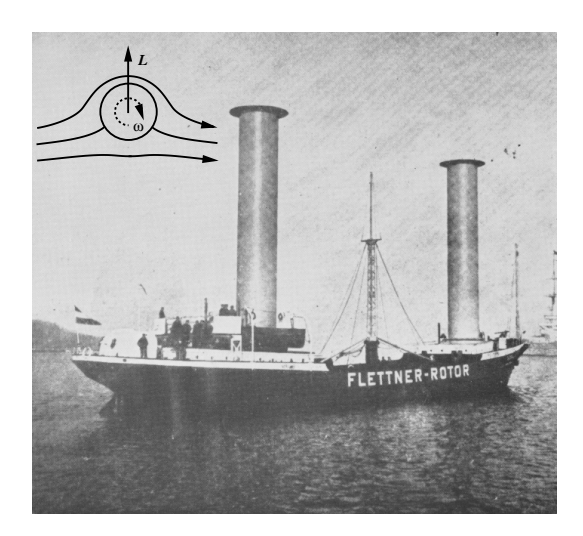
In 1922, A. Flettner embarked on the design of a wind-powered ship based on the Magnus effect. The work culminated in 1924 with the testing of this concept on the retrofitted German naval schooner *Buckau* (Figure 2a), which was later renamed the *Baden-Baden*. This large cargo ship (497 tons gross) set "sail" by way of the Magnus effect and two rotating cylindrical "rotors", each of which was 2.7m in diameter and 18m tall and driven to a maximum rotational velocity of 120 rpm by a total of 11 kW of electric power (Flettner [7, 8]). The *Buckau* was followed in 1926 by the retrofit of the *Barbara*. This larger ship (2077 tons gross) was fitted with three rotors, each approximately 4m in diameter and 17m tall and driven to a maximum rotational velocity of 150 rpm by a total of 56 kW of electric power (Dunn [9] and Leek [10]).

The available literature indicates that both ships exhibited a substantial amount of thrust from the rotors even under fairly light wind conditions and were not substantially destabilized by the rotors under heavy wind conditions. However, the rotors required wind to produce thrust, and were developed at a time in which fuel was fairly cheap and represented only a minor fraction of the cost of operating a merchant marine vessel. As a result, the fuel savings achieved was not deemed to warrant the expense and complexity introduced by the rotor mechanism by those in the merchant marine industry, and the idea was essentially abandoned. The rotor ships of the 1920s did, however, succeed in sparking the imagination of several budding engineers of that era—see, e.g., the artist's conception of possible future rotorships on the cover of the July 1933 issue of *Popular Science Monthly* (hereafter referred to as *PSM*) and several related novel designs in other issues of this popular magazine during the 1930s and 40s, including boats propelled by large, barrel-shaped rollers (July 1930 and May 1936), a "tractor boat" (Oct 1935), a human-propelled floating "hamster wheel" (Sep 1938), and a worm-gear ship propellor (May 1946). Though U.S. patents were granted on several such novel designs, most proved to be naive and inefficient in certain respects, and several were beyond the manufacturing capabilities of the era. Thus, many of these ideas were largely forgotten at the outbreak of WWII.

An interesting variation on the design of Flettner's cylinderical rotors was proposed by L. Lesh (see *PSM* July 1933), in which a surfboard-shaped rotor is used, thereby deriving both the torque to spin the rotors and the force to propel the ship from the wind itself. Another proposed variation (see *PSM* July 1934) employed three large spinning cones attached at their vertices at the top of a conventional mast. Neither design was advanced past the experimental stages. Related vertical "rotor" designs developed during the 1920s include the Savonius rotor and the more sophisticated Darrieus rotor. The Savonius rotor consists essentially of a barrel which has been cut in half by a plane containing the centerline, with the two halves reattached after being offset in the radial direction by the radius of the barrel. Credit for invention of the Savonius rotor officially goes to S.J. Savonius in circa 1924, but in fact may have been developed earlier by others (see Park [11]). The Darrieus rotor, invented by G.J.M. Darrieus in circa 1925, uses slender curved airfoil blades (arranged in a fashion that looks something like an eggbeater) to generate lift, creating torque about the vertical axis. Both of these rotors, though not seeing applications for ship propulsion, are in common use today as windmills (Park [11]).

The Turbosail[™], which works according to a principle related to that of the rotorships but with a pressurized interior of the large cylindrical sail and a computer-controlled downstream-blowing slot used to maintain attached flow on the leeward side of the sail (Charrier *et al.* [12]), was developed in 1982 by L. Malavard, B. Charrier and J.-Y. Cousteau and used on the Cousteau Society's ships *Moulin à Vent I* and *Alcyone* (Figure 2b). This innovative design (U.S. Patent No. 4630997) has proven to be reliable and efficient for wind propulsion of large ships. Slotted flaps (see, e.g., McCormick [13]) are the common aeronautical equivalent of this design.

Rotating cylinders may also be embedded in a surface with their axes aligned in the spanwise direction, exposing only a portion of the cylinders to the overlying flow, to effectively energize the near-wall flow and thereby delay or avoid separation. Contrary to much of the post-WWII literature on the subject, the idea appears to have been originally proposed by R. Thompson (see *PSM* Feb. 1932). However, it was first pursued in earnest by A. Alvarez-Calderon [2]. The first flight-test program implementing this idea took place in Peru, where a single-engine Ryan VZ-3RY was modified to incorporate such an embedded cylinder at the wing/flap junction (Figure 3) in an effort to design new low-speed short take-off/land (STOL) counter-insurgency aircraft (Brown [3]). The idea was studied further from 1968 to



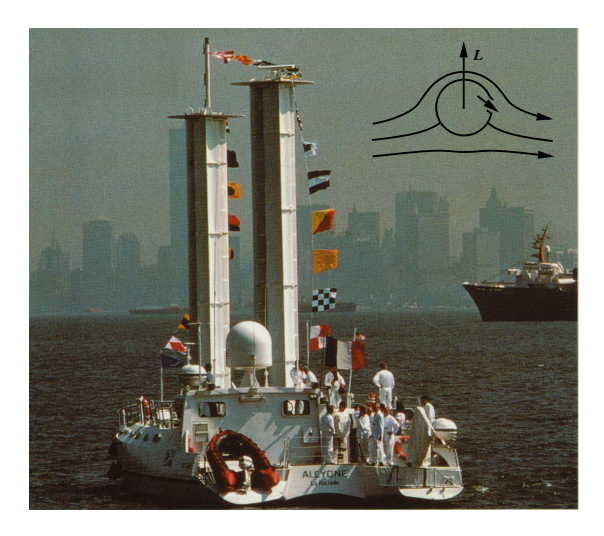


Figure 2: Evolution of cylindrical "sails" for ship propulsion: the rotating cylinders of Flettner's Buckau (circa 1924, shown left) and the Turbosail of the Cousteau Society's Alcyone (circa 1982, shown right). As depicted in the insets, Flettner's design achieves thrust via the Magnus effect, whereas the Cousteau design incorporates a downstreamblowing slot on the leeward side of the cylinder to maintain attached flow. Photographs from (left) Tokaty [1] and (right) the Cousteau Society, republished with permission.

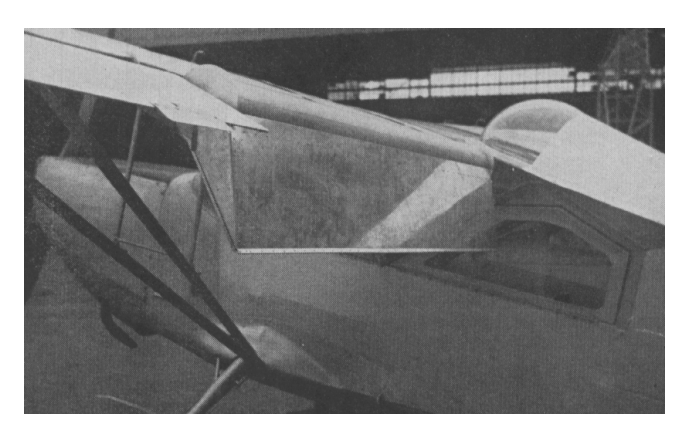


Figure 3: A Ryan VZ-3RY of the Peruvian Air Force, modified by Alvarez-Calderon [2] to use a rotating cylinder at the wing/flap junction in order to maintain attached flow when the flap is deflected. Photographs from Brown [3], republished with permission.



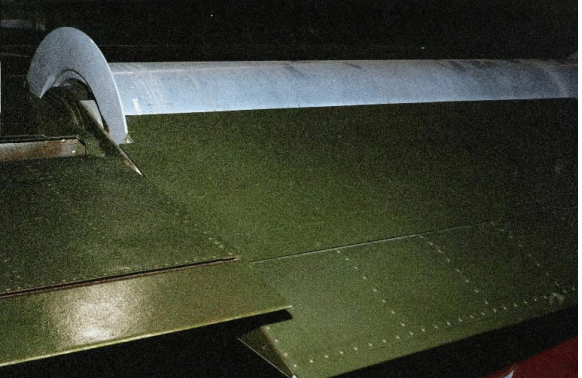


Figure 4: Follow-on tests to those in Peru were performed at NASA-Ames on this modified OV-10A, using essentially the same design (Cichy, Harris, & MacKay [4]). Note that the gap between the cylinder and the wing surface is extremely narrow in this implementation. Photographs by the author.

1976 at NASA-Ames Research Center (Cichy, Harris, & MacKay [4]). In this investigation, the embedded-cylinder idea was implemented and extensively tested on an OV-10A aircraft. Take-off and landing distances of less than 900 feet and a stall speed of less than 43 KIAS were obtained. This remarkable aircraft has recently been carefully restored and is now on static display at the Yankee Air Museum at Willow Run Airport in Ypsilanti, MI (Figure 4). Windtunnel tests have convincingly verified the effectiveness of this design for separation delay, as illustrated in Figure 5. R. Englar [14, 15] provides a thorough review of various embedded rotating cylinder designs and compares the performance of such designs with several other competing "circulation control" strategies (slotted flaps, blown flaps, jet flaps, etc.) for short takeoff and landing (STOL) applications. V. Modi [16] provides another excellent review of the literature related to embedded rotating cylinder designs.

As discussed in the Wright-Brothers' lecture of Goldstein [19], radical active flow control strategies, such as

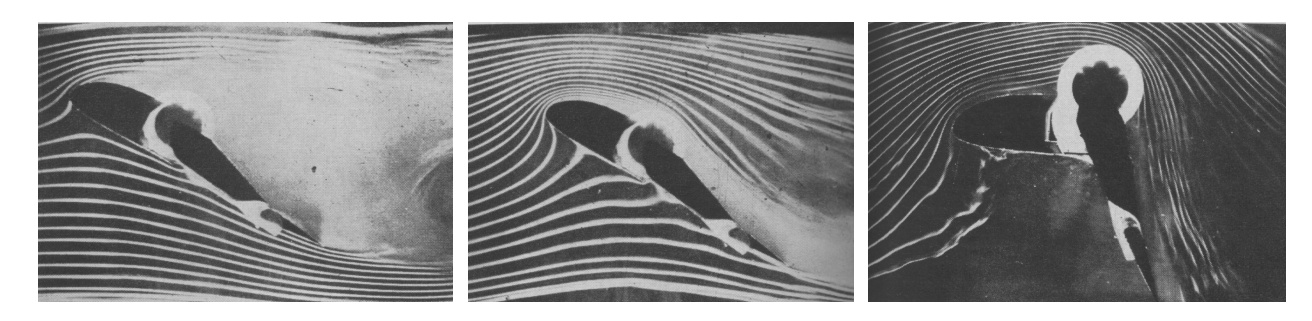


Figure 5: Wind tunnel tests of the embedded rotating-cylinder design, from Alvarez-Calderon [2], demonstrating large-scale separation with the cylinder stationary (left), and elimination of separation at the same flow conditions with the cylinder spinning (center); even at exaggerated flap deflections, maintaining attached flow is possible with a sufficiently high rotation rate of the cylinder (right). Republished with permission.

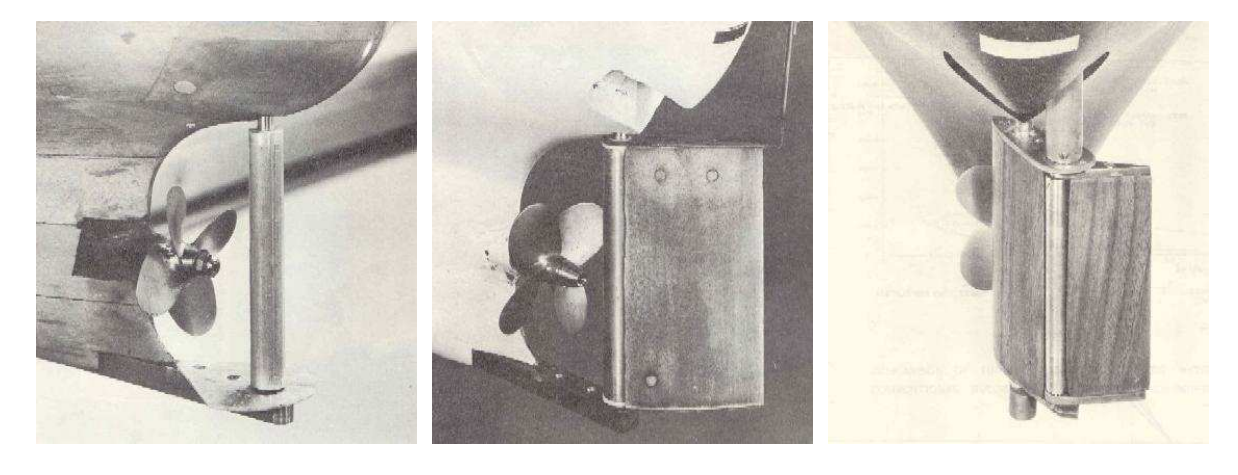


Figure 6: Various rudder designs employing both isolated and embedded rotating cylinders, from Steele & Harding [17]. Republished with permission.

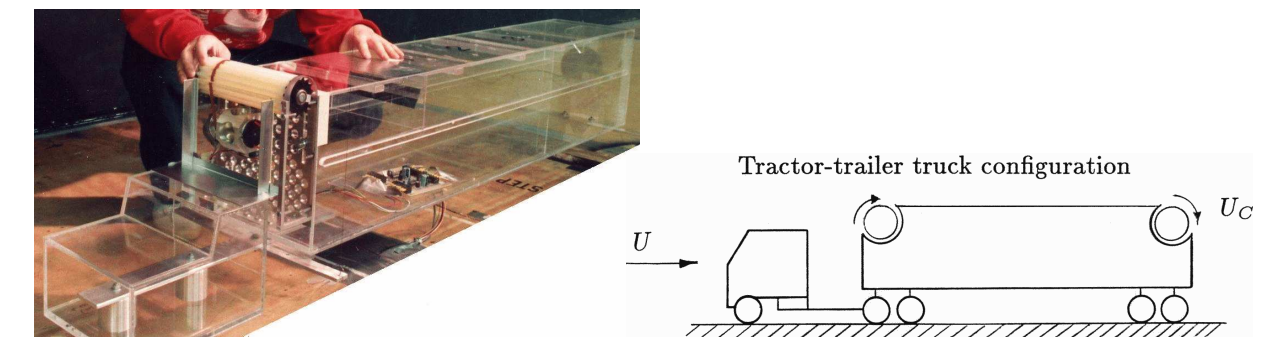


Figure 7: Wind tunnel tests of rotating-cylinder control of the flow over the leading/trailing edges of a tractor-trailer truck, by Modi, Fernando, & Yokomizo [18]. Republished with permission.

the incorporation of rotating cylinders or moving belts as discussed here, necessitate redesign of the airfoil shape in order to obtain maximum efficiency. Such redesign of the airfoil shape should be considered in future work. Other applications which have been proposed for similar embedded rotating-cylinder mechanisms include hydrofoils (Brooks [20]), ship rudders (Steele & Harding [17]; see Figure 6), diffusers (Tennant [21]), and tractor-trailer trucks (Modi, Fernando, & Yokomizo [18]; see Figure 7). It is straightforward to extend the surface area over which such a design has an effect simply by placing several embedded rotating cylinders in series, though it is not possible keep the surface flat while following this approach.

1.2 Approaches based on moving belts

The idea of using a moving belt to extend the effect imparted by an embedded rotating cylinder over a large surface area is also quite old. G.A. Tokaty [1], in his charming historical account *A History and Philosophy of Fluidmechanics*, reviews many of the early investigations on this topic, with emphasis on the contributions from the former Soviet Union (much of which never reached the western scientific literature). A photograph of (apparently) the first driven moving-belt mechanism for boundary layer drag reduction, developed by D.P. Riabouchinsky in 1914, appears in Tokaty's book. Sketches of several experimental designs by B.N. Your'yev (circa 1926) and Tokaty (circa 1937) for application of such a mechanism to airfoils also appear in this book. Tokaty reports that these designs achieved separation delay "up to about 25° of angle of attack", though the experimental data they obtained and photographs of the actual devices they constructed appear to be difficult to obtain in the west. H. Schlichting [22], in the seventh edition of his classic book *Boundary Layer Theory*, reviews further some of the early western literature on this and related topics.

In his Ph.D. thesis and several related short articles in *Comptes Rendus* (Favre [23, 24]), A. Favre documented a thorough experimental investigation of the effects a moving surface has on the aerodynamics of an airfoil. The moving-belt apparatus used on Favre's airfoil is illustrated in Figure 8, and representative flow visualizations are depicted in Figure 9. As illustrated in these figures, the designs tested were highly effective at inhibiting separation, yielding very high maximum lift coefficients at high angles of incidence (up to $C_{L,max} = 3.7$ at $\alpha = 55^{\circ}$), and maintaining attached flow even up to $\alpha = 115^{\circ}$.

After WWII, the focus in the field of aerodynamics seems to have shifted away from fundamental low-speed boundary-layer theory, and research on the moving-belt idea for boundary-layer control in the 50 years that followed is fairly sparse. In the study of Truckenbrodt [25], a laminar boundary layer is considered as it develops first over a stationary wall over its upstream portion, and then over a moving belt mechanism (similar to that depicted in Figure 1) in its downstream portion. The suitability of the moving-belt mechanism for separation delay is motivated by this analysis. Further analysis of a similar configuration in the turbulent regime is provided by Tennant & Yang [26], using both experiments and RANS computations using the Cebeci-Smith turbulence model.

In his book (first published in 1951), Schlichting ultimately dismissed the moving-belt approach quite pessimistically:

"With the exception of rotating cylinders, the idea of moving the solid wall with the stream can be realized only at the cost of very great complications as far as shapes other than cylindrical are concerned, and consequently, this method has not found much practical application."

An old idea nearly forgotten for half a century, the moving-belt mechanism for boundary-layer control has been re-introduced to the modern flow control community by Bechert, Hage, & Brusek [27]. In this work, a passively-driven moving-belt mechanism of essentially the same type as that shown in Figure 1 was constructed and installed on one of the walls of a channel flow, and careful drag reduction experiments were performed. Skin friction reductions of up to 9% were measured. Inspired by this result, Choi & Choi [28] performed computations of the effect of mounting a passively-driven moving-belt mechanism upstream of the separation points in a 2D cylinder flow at Re = 100, and found that separation could be delayed substantially, thereby reducing the total drag by up to 28% when 1/4 of the surface area of the cylinder was covered with the moving-belt mechanism. The ability of moving-belt mechanisms to obtain significant drag reduction and separation delay, as reported in these two papers, is in substantial agreement with the large body of previous work on this subject, as reported above. Significant separation delay caused by surface motion in the streamwise direction is also evident in two-phase flows, such as the flow of air past a drop of water or the flow of water past a bubble of air. In such flows, an internal Hill's spherical vortex arises due to the friction of the external flow, resulting in surface motion analogous to that imparted by a moving belt and concomitant drag reduction and separation delay (Panton [29], Sirignano [30]).

Despite these recently-published successes in drag reduction and separation delay with the moving-belt mechanism, the pessimism expressed by Schlicting in this mechanism 50 years ago still appears to be prevalent with many flow control researchers today. For example, Gad-el-Hak [31], in his recent book *Flow Control*, states

"From a practical point of view, wall motion for body shapes other than circular cylinders or spheres is prohibitively complicated, ..."

The pessimism expressed in such comments might be unwarranted. For example, for applications to flat wall segments, the "complications" involved in building a moving-belt mechanism, such as that shown in Figure 1, in fact seem quite manageable (four bearings, two rollers, and a belt) when compared with many flow control strategies recently proposed, many of which necessitate micro-electro-mechanical systems (MEMS), which are typically quite fragile. Further discussion of the practical matters of this mechanism is deferred to §5.5.

Perhaps one of the reasons for the pessimism in the moving-belt approach is the daunting prospect of getting a large-scale belt to move over thin rollers at a hundred miles per hour or more without vibrating, as would be necessary in the application of this concept to aircraft operating in the high subsonic range. However, there is now a large (and growing) niche market for small unmanned aerial vehicles (UAVs) and unmanned undersea vehicles (UUVs) which operate at low speeds and (also due to their small size) at low Reynolds numbers. In such applications, sustaining laminar attached flow is quite possible, and the construction of the belt mechanism appears to be feasible due to the low aerodynamic loads involved. Thus, in contrast to the recent investigations by Bechert, Hage, & Brusek [27] and Choi & Choi [28], the bulk of the present paper focuses on laminar attached flow, targeting UAV/UUV and "microfluidic" applications in which viscous effects are dominant and the efficiency of traditional, higher Reynolds number designs is degraded. This leads to a number of novel design concepts.

Other strategies that have used in-plane wall motions to control wall-bounded flows include

- open-loop strategies involving periodic spanwise wall oscillations (see, e.g., Jung, Mangiavacchi, & Akhavan [32]; Sendstad & Moin [33]; Laadhari, Skandaji, & Morel [34]; Choi, DeBisschop, & Clayton [35]),
- wall-normal vorticity actuation strategies by coordinated feedback control of flush-mounted MEMS micromotors using the OGY chaos control technique (Keefe [36]), and
- feedback strategies targeting global stabilization or destabilization of the nonlinear Navier-Stokes equation (Balogh, Liu, & Krstic [37]; Aamo, Krstic, & Bewley [38]).

It should also be mentioned that moving belts have been useful in several fundamental turbulence investigations to study "shear-free" turbulent boundary layers (see, e.g., Uzkan & Reynolds [39]; Thomas & Hancock [40]; Aronson,

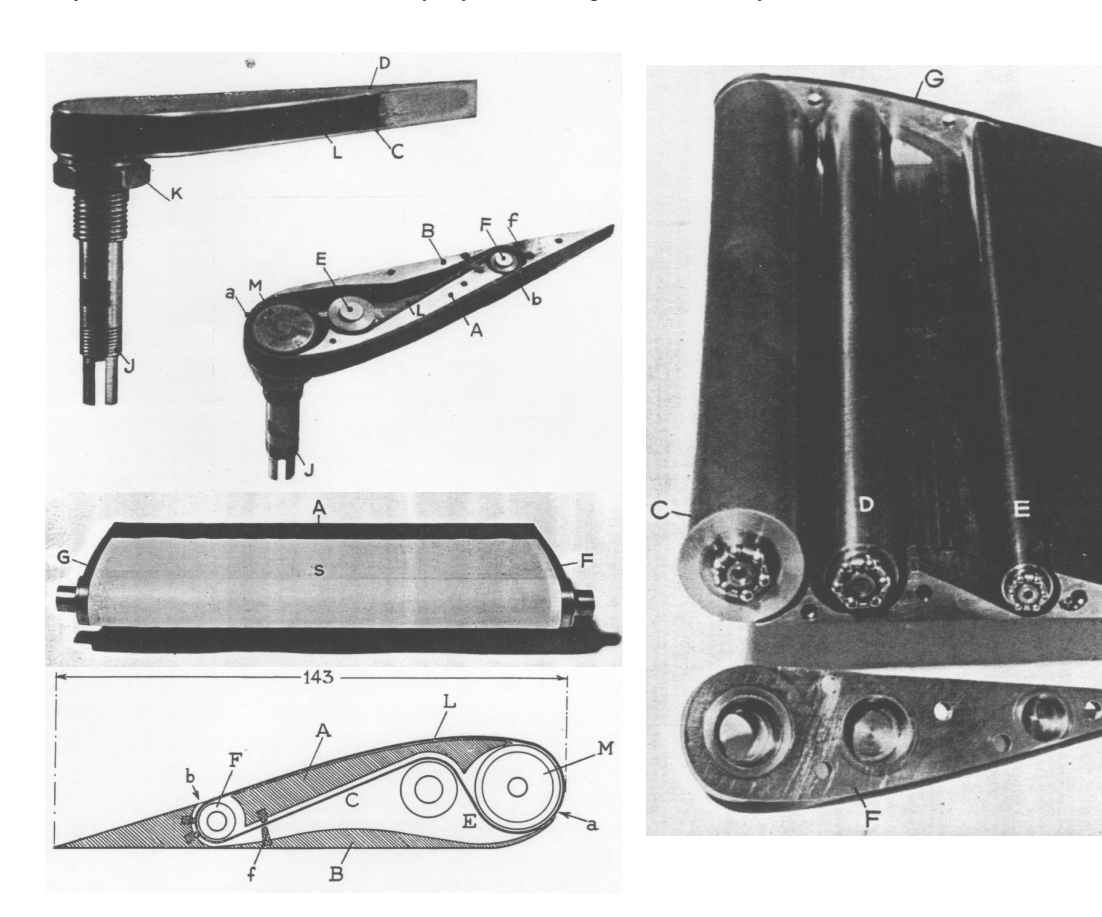


Figure 8: Two moving-belt mechanisms tested by Favre [23]: a narrow-span configuration (upper-left) and a wide-span configuration, shown here with the belt installed (center-left) and the belt removed (right). The two designs have similar cross-sectional configurations (lower-left); note in particular that the gap between the belt and the substructure of the airfoil is extremely narrow over extensive regions in these implementations. Republished with permission.

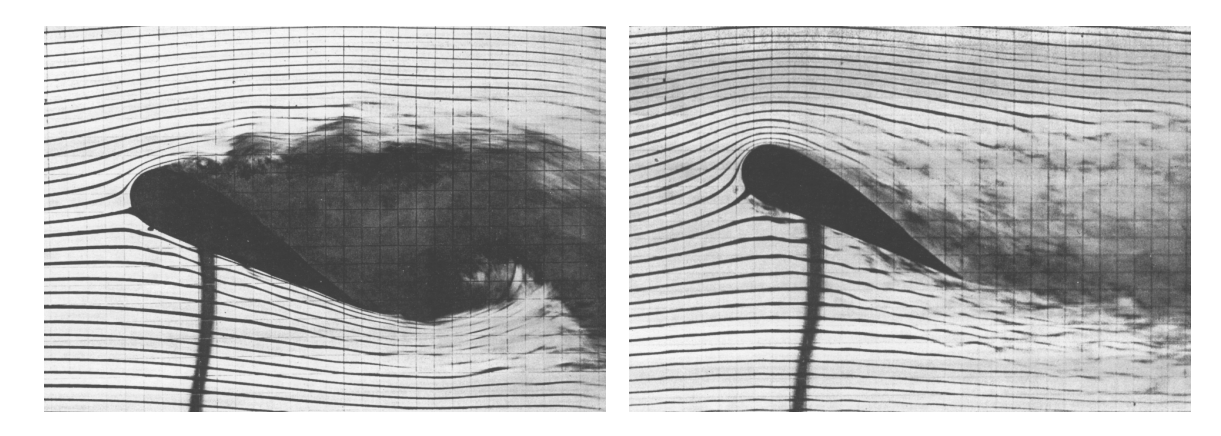


Figure 9: One of several wind-tunnel tests of moving-belt mechanisms by Favre [23], demonstrating large-scale separation with the belt stationary (left), and elimination of separation at the same test conditions with the belt moving (right). Republished with permission.

Johansson, & Löfdahl [41]), and are now fairly standard test equipment to account for the motion of the groundplane with respect to the vehicle in automotive wind tunnel experiments (see, e.g., Katz [42]).

Motivated by the several successes of flow control strategies based, for example, on simple rotating cylinders, together with the recent advances in material technology which appear to make the fabrication of reliable low-friction moving-belt mechanisms now possible and the rising costs of fuel and new applications (such as UAVs) driving radical departures from "standard" vehicle configurations, it appears to be an appropriate time to revisit the idea of using moving belts for the control of wall-bounded flows in both aeronautical and maritime applications. Though it is true that, in theory, the feedback control strategies which MEMS devices enable are sometimes the most energetically efficient means of stabilizing a fluid system (see, e.g., the recent reviews of progress in this direction in Gad-el-Hak [43] and Bewley [44]), the promising opportunities for simple mechanisms for passive or open-loop active control of wall-bounded flows should not be overlooked. The moving-belt mechanism illustrated in Figure 1 provides just such an opportunity. With the present paper, we seek to both quantify the effectiveness of this flow control strategy in the laminar regime and suggest new applications for this mechanism which have previously been unexplored.

2 Laminar channel flow

2.1 Fully developed channel-flow profile with moving-belt mechanism

The geometry considered first is shown in Figure 1. Assuming laminar flow with sufficiently large L_x , we may compute the 1D profiles of this flow analytically. Given the channel half-width δ , the depth of the cavity d = 2r + h, and the radius of the rollers r, the velocity profiles illustrated in Figure 1 may be parameterized as:

where u_w is the velocity of the belt and a, b, and c are coefficients to be determined. Note that, by construction with this parameterization,

$$u(y = \pm \delta) = u_w$$
 in Ω , $u_a(y_a = r) = u_w$ in Ω_a , $u_a(y_a = -r) = -u_w$ in Ω_a , $u_b(y_b = 0) = 0$ in Ω_b ,

and the mass flux in Ω_a is zero. We seek to find a, b, c, and u_w such that

- A. the mass flux per unit volume of the channel flow in Ω is some prescribed value U_B (note that U_B is also referred to as the "bulk velocity"),
- B. the mass flux in Ω_b is zero, modeling zero entrainment of the flow from Ω into Ω_b around the ends of the rollers (this condition will later be relaxed),

C.
$$u_b(y_b = h) = -u_w$$
 in Ω_b , and

D. the sum of the forces on the belt is zero.

Assuming zero torques applied at the roller supports and no losses due to bearing friction or belt deformation, these four conditions lead immediately to four linear equations in the four unknowns $\{a,b,c,u_w\}$:

$$\begin{split} \frac{1}{2\delta} \int_{-\delta}^{\delta} \left[u_w + a(\delta^2 - y^2) \right] dy &= U_B, \\ \int_{0}^{h} \left[b y_b - c y_b^2 \right] dy_b &= 0, \\ b h - c h^2 &= -u_w, \\ \mu \frac{d}{dy} \left[u_w + a(\delta^2 - y^2) \right]_{y=-\delta} - \mu \frac{d}{dy_a} \left[u_w \frac{y_a}{r} \right]_{y_a=r} - \mu \frac{d}{dy_a} \left[u_w \frac{y_a}{r} \right]_{y_a=-r} + \mu \frac{d}{dy_b} \left[b y_b - c y_b^2 \right]_{y_b=h} &= 0, \end{split}$$

where μ is the viscosity of the fluid. (Note also that ρ is defined as the density of the fluid, ν is the kinematic viscosity of the fluid, and $\nu = \mu/\rho$.) These equations may be rewritten as

$$\frac{2\delta^2 a}{3} + u_w = U_B,$$

$$\frac{h^2 b}{2} - \frac{h^3 c}{3} = 0,$$

$$hb - h^2 c + u_w = 0,$$

$$2\delta a + b - 2hc - \frac{2u_w}{r} = 0,$$

or in matrix form as

$$\begin{pmatrix} 2\delta^2/3 & 0 & 0 & 1\\ 0 & h^2/2 & -h^3/3 & 0\\ 0 & h & -h^2 & 1\\ 2\delta & 1 & -2h & -2/r \end{pmatrix} \begin{pmatrix} a\\b\\c\\u_w \end{pmatrix} = \begin{pmatrix} U_B\\0\\0\\0 \end{pmatrix}.$$

Defining $f = 3hr + 4\delta r + 2h\delta$, the solution is

$$a = \frac{3U_B(2r+h)}{\delta f}, \quad b = \frac{6U_B r}{f}, \quad c = \frac{9U_B r}{h f}, \quad \text{and} \quad u_w = \frac{3hU_B r}{f}.$$
 (2)

For example, taking $\delta = h = r = U_B = 1$, we find that a = 1, b = 2/3, c = 1, and the belt velocity $u_w = 1/3$.

2.2 Drag reduction

Inserting the solution for a, b, c, and u_w into the parameterizations of the velocity profiles, it is seen that all three profiles simply scale linearly with the bulk velocity U_B . Also, we may choose to geometrically scale all lengths in the problem by δ . Thus, when properly scaled, the velocity profiles derived above are independent of the Reynolds number based on the bulk velocity and channel half width, $Re_B \triangleq U_B \delta/\nu$, so long as the Reynolds number is sufficiently low that the flow is laminar. (Analogously, for the laminar boundary-layer cases examined in §3 & 4, we will determine similarity profiles which are independent of the Reynolds number based on the free-stream velocity and displacement thickness, $Re_{\delta^*} \triangleq U_\infty \delta^*/\nu$, so long as the flow is laminar.) In fact, there are just two geometric parameters which characterize the profiles in the laminar channel-flow case, which we define to be the ratio of the roller radius to the cavity depth, r/d, and the ratio of the cavity depth to the channel half width, d/δ . We therefore now study the percent drag reduction possible with this moving-belt mechanism as a function of these parameters.

Defining the control volume as the channel-flow domain Ω only, the drag force per unit area, D, exerted by the channel flow onto the lower belt (and thus, by the sum of the forces exerted on the roller supports and the walls of Ω_b , the force per unit area exerted on the supporting structure below the channel) is given by

$$D = \mu \frac{d}{dy} \left[u_w + a(\delta^2 - y^2) \right]_{y = -\delta} = 2\mu \delta a.$$

Normalizing this equation by the drag when the belt is stationary, $D_0 = 3\mu U_B/\delta$, the drag as a function of r/d and d/δ is plotted in Figure 10. The normalized roller size r/d = 0.25 is seen to provide the greatest drag reduction for all values of d/δ .

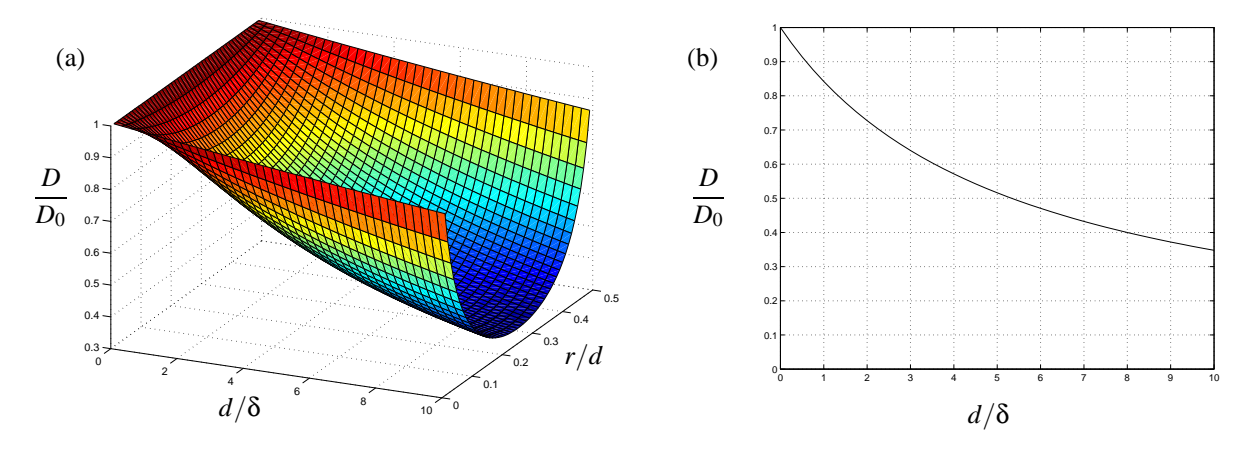


Figure 10: Drag reduction of plane channel flow when the passively-driven belt mechanism is installed, assuming no entrainment of the main flow into the lower cavity. (a) Normalized drag as a function of cavity depth and roller size. (b) Normalized drag as a function of cavity depth for the optimum roller size r/d = 0.25. Assuming the flow is laminar, the result shown is independent of Reynolds number.

The percent drag reduction possible via this strategy increases monotonically as a function of cavity depth, but is modest for reasonable cavity depths. Neglecting bearing friction and the energy lost in deforming the belt, only 17.8% drag reduction is possible for $d = \delta$, and 48.4% drag reduction is possible for $d = 5 \delta$. Both of these cavity depths would probably be considered as "large" from the implementation perspective. Indeed, for the channel-flow application, it would make much more sense just to increase the channel half width δ without putting the belt mechanism in the way. Symmetrically increasing the channel half width δ by an amount $d = \delta$ at the upper and lower walls without introducing moving-belt mechanisms, while maintaining the total mass flux constant, results in a 75% drag reduction (over four times better drag reduction than the configuration proposed in Figure 1). Thus, the present study on the drag reduction and stability enhancement characteristics of the moving-belt mechanism applied to channel flows is provided for the sole purpose of introducing these effects in a simple environment in which the fully-developed flow is available analytically and is invariant in the streamwise coordinate. The engineering benefit of implementing the moving-belt mechanism to achieve these effects will become apparent in §3 & 4, where we discuss the application of this mechanism to boundary layers.

2.3 Stability enhancement

As shown by Orszag [45], the parabolic laminar channel-flow profile

$$u = \frac{3U_B}{2\delta^2} \left(\delta^2 - y^2\right) \tag{3}$$

is a linearly stable solution to the Navier-Stokes equation with no-slip boundary conditions for $Re_B \triangleq U_B \delta/\nu < Re_{B,LS}$, and is a linearly unstable solution for $Re_B > Re_{B,LS}$, where the critical bulk Reynolds number for linear stability of the channel flow is $Re_{B,LS} = 3848$. Note that this corresponds to a critical centerline Reynolds number of $Re_{c,LS} = 5772$, where $Re_c \triangleq U_c \delta/\nu$ and the centerline velocity of laminar channel flow is $U_c = \frac{3}{2}U_B$. Nonlinear instability of channel flows with sufficiently large initial perturbations or applied external disturbances is often seen at subcritical bulk Reynolds numbers which are well below $Re_{B,LS}$. Both experiments and computations verify that global stability of laminar channel flow is consistently seen for $Re_B < Re_{B,GS}$, where $Re_{B,GS} \approx 670$ (Schmid & Henningson [46]), though the bulk Reynolds number for global stability of this system has not been determined very precisely.

When the moving-belt boundary conditions are imposed, the question of stability of the resulting parabolic flow in Ω , given in (1), can easily be reduced to the question of stability in the no-slip case (3) for a modified value of the bulk velocity U_B . To illustrate, consider the simple change of variables

$$\tilde{u} \stackrel{\triangle}{=} u - u_w. \tag{4}$$

This change of variables reduces the profile in Ω given in (1) to a profile of the form

$$\tilde{u} = \frac{3\tilde{U}_B}{2\delta^2} \left(\delta^2 - y^2 \right),\tag{5}$$

with what we define as an effective bulk velocity \tilde{U}_B of

$$\tilde{U}_B \triangleq U_B - u_w$$

corresponding to an effective bulk Reynolds number \widetilde{Re}_B of

$$\widetilde{Re}_{B} \stackrel{\triangle}{=} \frac{\widetilde{U}_{B}\delta}{V} = \frac{(U_{B} - u_{w})\delta}{V} = Re_{B} - \frac{u_{w}\delta}{V}.$$
 (6)

Note that the Navier-Stokes equation remains unchanged under this change of variables, and its boundary conditions are made homogeneous. Thus, the question of stability of (5) at a particular value of \tilde{U}_B is equivalent to the question of stability of (3) at that value of U_B , which is a solved problem. Converting back to the original coordinate system, it is thus seen that the critical Reynolds numbers in the moving belt case are

$$Re_{B,LS} = 3848 + \frac{u_w \delta}{v}, \qquad Re_{B,GS} = 670 + \frac{u_w \delta}{v}.$$

Inserting for u_w from (2) at the corresponding critical Reynolds numbers and rearranging yields

$$Re_{B,LS} = 3848 \left(1 + \frac{3}{2} \frac{d}{\delta} \left(1 - 2 \frac{r}{d} \right) \frac{r}{d} \right) = 3848 \left(1 + \frac{3}{2} \frac{d}{\delta} \frac{1}{g} \right), \qquad Re_{B,GS} = 670 \left(1 + \frac{3}{2} \frac{d}{\delta} \frac{1}{g} \right),$$

where $g \triangleq [(1-2r/d)r/d]^{-1}$. Thus, for a given value of r/d, the critical Reynolds numbers for instability of the parabolic profile in Ω increase linearly with d/δ , as illustrated in Figure 11. The value of r/d which minimizes g, and therefore maximizes these critical Reynolds numbers, is r/d = 0.25, resulting in g = 8.

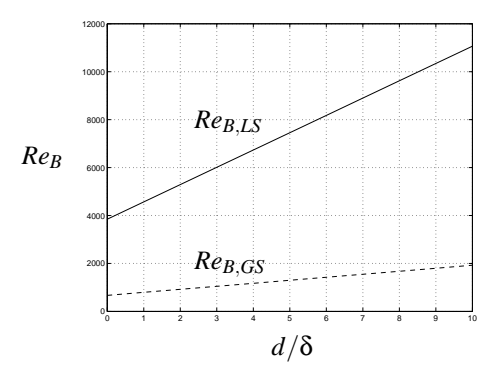


Figure 11: Critical bulk Reynolds numbers for stability of the channel flow in Ω in the system depicted in Figure 1 as a function of cavity depth for r/d=0.25. For bulk Reynolds numbers $Re_B \triangleq U_B \delta/\nu$ below $Re_{B,LS}$ (solid line), the laminar flow in Ω is linearly stable, and for bulk Reynolds numbers Re_B below $Re_{B,GS}$ (dashed line), the laminar flow in Ω is globally stable.

As shown in Potter [47], a small Couette component is sufficient to linearly stabilize plane Couette-Poiseuille flow. In particular, Potter showed that, assuming a laminar flow profile u(y) between two plane walls at y = 0 and y = 1, all flows for which

$$|u(1) - u(0)| > 0.7 \left| u(0.5) - \frac{u(1) + u(0)}{2} \right|$$
 (7)

are linearly stable to infinitesimal disturbances for all Reynolds numbers. As the flows in both Ω_a and Ω_b (see Figure 1) satisfy Potter's inequality (7), these flows are linearly stable.

It is well known that, due to a variety of so-called "bypass" mechanisms, transition in plane channel flows with no-slip boundary conditions typically occurs for Re_B well below $Re_{B,LS}$ even when the initial perturbation or applied external disturbances are fairly "small" (for a recent review of such transition mechanisms, see Schmid & Henningson [46]). Using the above-described change of variables, the wide literature on such mechanisms extends directly to the region denoted Ω in the present configuration (Figure 1) at the effective Reynolds number defined in (6).

Related bypass mechanisms are also possible in the Couette flow in Ω_a and in the zero-net mass-flux Couette-Poiseuille flow with one stationary wall in Ω_b (see Figure 1). (In the case of Couette flow, Romanov [48] established a lower bound on the domain of convergence of the laminar flow state as a function of Reynolds number.) In fact, as the effective Reynolds number increases with d/δ in Ω_a and Ω_b but decreases with d/δ in Ω for a fixed value of U_B , for sufficiently large d/δ bypass transition will actually occur in Ω_a and Ω_b for lower values of U_B than that necessary to excite bypass transition in Ω , even though the laminar flows in Ω_a and Ω_b are linearly stable for all Reynolds numbers. The phenomena of bypass transition is thus significant for all three flow regions, and should be characterized carefully before implementation in a practical configuration if laminar flow is desired for values of U_B which are not small.

2.4 Power extraction or addition

Utilization of the moving-belt mechanism shown in Figure 1 for either the extraction of power from the flow (for example, for the generation of electricity) or the addition of power to the flow (that is, to pump the fluid) is straightforward simply by applying electric generators or motors to the roller supports. In the following three subsections, we analyze the system efficiency of three different configurations for the power extraction (electricity generation) application. In the subsection that follows (§2.4.4), we consider the system efficiency of these three configurations for the power addition (pumping) application.

2.4.1 Power extraction: configuration #1

In the symmetric configuration depicted in Figure 1 for a given belt speed u_w (which may be controlled by adjusting the load on the generators), the velocity profiles of the main flow in Ω and the recirculating flows in the fluid-filled cavities Ω_a and Ω_b are given by (1), where a, b, and c follow from conditions A, B, and C of §2.1:

$$\begin{pmatrix} 2\delta^2/3 & 0 & 0 \\ 0 & h^2/2 & -h^3/3 \\ 0 & h & -h^2 \end{pmatrix} \begin{pmatrix} a \\ b \\ c \end{pmatrix} = \begin{pmatrix} U_B - u_w \\ 0 \\ -u_w \end{pmatrix}.$$

The solution of this system is:

$$a = \frac{3(U_B - u_w)}{2\delta^2}, \quad b = \frac{2u_w}{h}, \quad c = \frac{3u_w}{h^2}.$$
 (8)

Instead of applying the zero-torque condition at the roller supports (condition D) as done in §2.1, we now seek to maximize the efficiency by which we may extract power from the flow with the moving-belt mechanisms by appropriate selection of $0 < u_w/U_B < 1$ and $d/\delta > 0$.

The total power extracted by this system is equal to twice the power extracted by the lower belt, which is just equal to the belt velocity times the total tangential force on the belt. Thus, normalizing by the channel width, the power output extracted by the belts per unit volume of the channel, \mathcal{P}_{belt} , is:

$$\begin{split} \mathcal{P}_{\text{belt}} &= \frac{2u_w \mu}{2\delta} \left(\frac{d}{dy} \left[u_w + a(\delta^2 - y^2) \right]_{y=-\delta} - \frac{d}{dy_a} \left[u_w \frac{y_a}{r} \right]_{y_a=r} - \frac{d}{dy_a} \left[u_w \frac{y_a}{r} \right]_{y_a=-r} + \frac{d}{dy_b} \left[b y_b - c y_b^2 \right]_{y_b=h} \right) \\ &= \frac{u_w \mu}{\delta} \left(2\delta a + b - 2hc - \frac{2u_w}{r} \right). \end{split}$$

The power input per unit volume of the flow in the channel, \mathcal{P}_{flow} , is simply the bulk velocity times minus the mean pressure gradient:

$$\mathcal{P}_{\text{flow}} = U_B \left(-\frac{dp}{dx} \right) = \frac{U_B \mu}{2\delta} \left(\frac{du}{dy} \Big|_{y=-\delta} - \frac{du}{dy} \Big|_{y=\delta} \right) = 2\mu U_B a.$$

Thus, combining the expressions for the velocity profiles (8) with the expressions for \mathcal{P}_{belt} and \mathcal{P}_{flow} , the efficiency η of the power extraction by this configuration is

$$\eta = \frac{\mathcal{P}_{\text{belt}}}{\mathcal{P}_{\text{flow}}} = \frac{(u_w \mu / \delta)(2\delta a + b - 2hc - 2u_w / r)}{2\mu U_B a} = \frac{\frac{u_w}{U_B} \left[3\left(1 - \frac{u_w}{U_B}\right) - 2g\frac{u_w}{U_B}\frac{\delta}{d} \right]}{3\left(1 - \frac{u_w}{U_B}\right)}.$$
 (9)

The maximum efficiency for a given belt speed and cavity depth is found by minimizing g by selecting r/d=0.25, resulting in g=8. For this value of g, the efficiency η is plotted in Figure 12 as a function of u_w/U_B for several values of d/δ . It is seen that large values of d/δ are required to achieve over 30% efficiency in this design. Further, by setting $\partial \eta/\partial u_w=0$ and solving for u_w , it is easily shown that the maximum efficiency for a given cavity depth is given by $u_w/U_\infty=1-\sqrt{2g}/\sqrt{2g+3d/\delta}$, as marked by the asterisks in Figure 12.

2.4.2 Power extraction: configuration #2

If the flow in the channel is of water, and the cavities are installed only on the upper surface of the channel as shown in Figure 13, then the cavities may be filled with pressurized air at approximately the local pressure of the fluid in the channel. Note that the buoyancy of the air essentially traps it in the upper cavities. As the viscosity of air is only about 1% that of water, this is an effective strategy to minimize the losses due to the recirculating fluid within the driven-belt mechanisms. Note also, however, that the pressure of the flow in the channel decreases significantly as the flow evolves

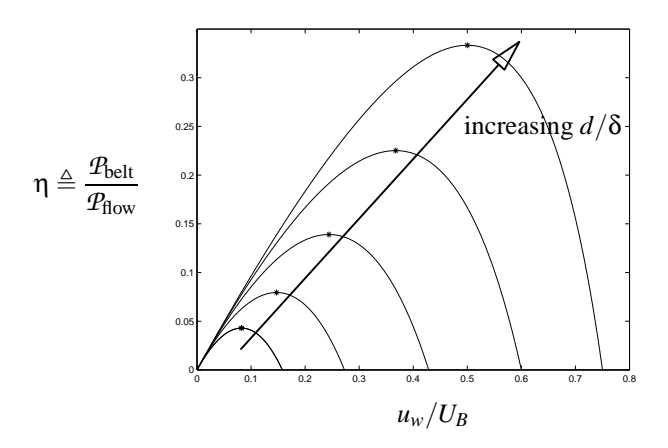


Figure 12: Efficiency of configuration #1 (depicted in Figure 1) for power extraction from a channel flow with the moving-belt mechanism as a function of u_w/U_B for $d/\delta = 1, 2, 4, 8, 16$ with r/d = 0.25.

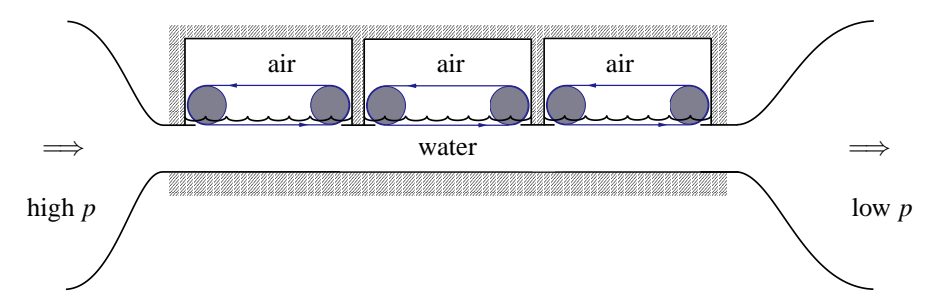


Figure 13: Configuration #2 for generation of electric power. Pressurized air is added to each cavity to just submerge the lower section of each belt, thereby minimizing losses due to the recirculating fluid within the driven-belt mechanisms.

downstream and power is extracted. Thus, if one chooses to fill the upper cavities with air, several separate cavities should be used to contain the upper belt mechanisms, with the air in each cavity at a different pressure, in order to minimize the normal load on the belts and the leakage and sloshing due to pressure differentials.

With this strategy, the peak efficiency may be estimated simply by neglecting the losses in the upper cavities. In this case, the flow profile in the main channel may be parameterized as

$$u = u_w \frac{\delta + y}{2\delta} + a(\delta^2 - y^2)$$
 with $-\delta < y < \delta$ in Ω (Couette-Poiseuille flow).

Setting the bulk velocity of the flow to U_B results in

$$\frac{1}{2\delta} \int_{-\delta}^{\delta} u \, dy = \frac{u_w}{2} + \frac{2\,\delta^2\,a}{3} = U_B \qquad \Rightarrow \qquad a = \frac{3}{4\delta^2} (2U_B - u_w).$$

The power extracted by the belt per unit volume of the channel may be estimated simply by taking the velocity of the belt times the tangential force on the belt per unit area, normalized by the channel width:

$$\mathcal{P}_{\text{belt}} = -\frac{u_w \mu}{2\delta} \frac{d}{dy} \left[u_w \frac{\delta + y}{2\delta} + a(\delta^2 - y^2) \right]_{y=\delta} = \frac{\mu u_w}{2\delta^2} (3U_B - 2u_w).$$

The power input per unit volume of the flow is, again, just the bulk velocity times minus the mean pressure gradient:

$$\mathcal{P}_{\text{flow}} = U_B \left(-\frac{dp}{dx} \right) = \frac{U_B \mu}{2\delta} \left(\frac{du}{dy} \Big|_{y=-\delta} - \frac{du}{dy} \Big|_{y=\delta} \right) = \frac{3\mu U_B}{2\delta^2} (2U_B - u_w).$$

The efficiency of the power extraction by this configuration is thus

$$\eta = \frac{\mathcal{P}_{\text{belt}}}{\mathcal{P}_{\text{flow}}} = \frac{u_w (3 - 2u_w / U_B)}{3U_B (2 - u_w / U_B)}.$$
(10)

By setting $\partial \eta / \partial u_w = 0$ while requiring that $u_w < 2U_B$ so that \mathcal{L}_{flow} is positive, it is easily shown that the maximum efficiency for this design is attained by taking the belt velocity $u_w = U_B$, for which we obtain $\eta_{max} = 1/3$.

2.4.3 Power extraction: configuration #3

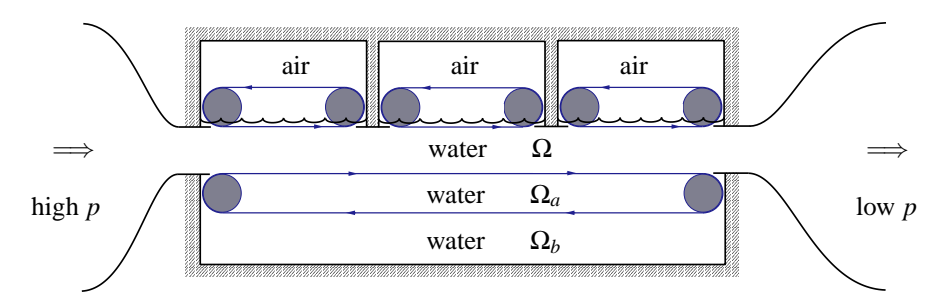


Figure 14: Configuration #3 for generation of electric power, combining the ideas of air-filled upper cavities and water-filled lower cavities.

Though filling the upper cavities with air, as done in Configuration #2 depicted in Figure 13, was an effective strategy to minimize the losses due to the recirculating fluid within the upper driven-belt mechanisms, a significant penalty was paid for extracting power from only one wall of the channel, and the resulting peak efficiency of the power extraction was only 33%. We now consider the asymmetric configuration shown in Figure 14, in which the lower cavities are filled with water, as in Configuration #1, and the upper cavities are filled with air, as in Configuration #2. With this strategy, the peak efficiency may be computed by combining the analysis techniques of the two previous sections. In this case, the flow profiles in the channel flow Ω and the lower cavities Ω_a and Ω_b (see Figure 14) may be parameterized as

$$\begin{split} u &= u_{lw} \frac{\delta - y}{2\delta} + u_{uw} \frac{\delta + y}{2\delta} + a(\delta^2 - y^2) & \text{with} \quad -\delta < y < \delta \quad \text{in } \Omega \quad \text{(Couette-Poiseuille flow)}, \\ u_a &= u_{lw} \frac{y_a}{r} & \text{with} \quad -r < y_a < r \quad \text{in } \Omega_a \quad \text{(Couette flow)}, \\ u_b &= b y_b - c y_b^2 & \text{with} \quad 0 < y_b < h \quad \text{in } \Omega_b \quad \text{(Couette-Poiseuille flow)}, \end{split}$$

where u_{lw} is the velocity of the lower belt, u_{uw} is the velocity of the upper belt, and a, b, and c follow from conditions A, B, and C of §2.1:

$$\begin{pmatrix} 2\delta^2/3 & 0 & 0 \\ 0 & h^2/2 & -h^3/3 \\ 0 & h & -h^2 \end{pmatrix} \begin{pmatrix} a \\ b \\ c \end{pmatrix} = \begin{pmatrix} U_B - (u_{lw} + u_{uw})/2 \\ 0 \\ -u_{lw} \end{pmatrix}.$$

The solution of this system is:

$$a = \frac{3[U_B - (u_{lw} + u_{uw})/2]}{2\delta^2}, \quad b = \frac{2u_{lw}}{h}, \quad c = \frac{3u_{lw}}{h^2}.$$
 (11)

We now seek to maximize the efficiency by which we may extract power from the flow by appropriate selection of both u_{lw} and u_{uw} . The total power extracted by the belts per unit volume of the channel is

$$\begin{split} \mathcal{P}_{\text{belt}} &= -\frac{u_{uw}\mu}{2\delta} \frac{d}{dy} \left[u_{lw} \frac{\delta - y}{2\delta} + u_{uw} \frac{\delta + y}{2\delta} + a(\delta^2 - y^2) \right]_{y=\delta} + \\ & \frac{u_{lw}\mu}{2\delta} \left(\frac{d}{dy} \left[u_{lw} \frac{\delta - y}{2\delta} + u_{uw} \frac{\delta + y}{2\delta} + a(\delta^2 - y^2) \right]_{y=-\delta} - \\ & \frac{d}{dy_a} \left[u_{lw} \frac{y_a}{r} \right]_{y_a=r} - \frac{d}{dy_a} \left[u_{lw} \frac{y_a}{r} \right]_{y_a=-r} + \frac{d}{dy_b} \left[b y_b - c y_b^2 \right]_{y_b=h} \right) \\ & = -\frac{\mu (u_{uw} - u_{lw})^2}{4\delta^2} + (u_{uw} + u_{lw})\mu a + \frac{u_{lw}\mu}{2\delta} \left(b - 2hc - \frac{2u_{lw}}{r} \right). \end{split}$$

As before, the power input per unit volume of the flow in the channel is:

$$\mathcal{P}_{\text{flow}} = U_B \left(-\frac{dp}{dx} \right)$$

$$= \frac{U_B \mu}{2\delta} \left(\frac{d}{dy} \left[u_{lw} \frac{\delta - y}{2\delta} + u_{uw} \frac{\delta + y}{2\delta} + a(\delta^2 - y^2) \right]_{y=-\delta} - \frac{d}{dy} \left[u_{lw} \frac{\delta - y}{2\delta} + u_{uw} \frac{\delta + y}{2\delta} + a(\delta^2 - y^2) \right]_{y=\delta} \right)$$

$$= 2\mu U_B a.$$

The efficiency of the power extraction by this configuration is thus

$$\eta = \frac{\mathcal{P}_{\text{belt}}}{\mathcal{P}_{\text{flow}}} = \frac{-\mu(u_{uw} - u_{lw})^2/(4\delta^2) + (u_{uw} + u_{lw})\mu a + u_{lw}\mu(b - 2hc - 2u_{lw}/r)/(2\delta)}{2\mu U_B a}
= \frac{-(u_{uw} - u_{lw})^2/(4U_B^2) + 3[1 - (u_{uw} + u_{lw})/(2U_B)](u_{uw} + u_{lw})/(2U_B) - (\delta/d)g u_{lw}^2}{3[1 - (u_{uw} + u_{lw})/(2U_B)]}.$$
(12)

Again, the peak efficiency is obtained by minimizing g by selecting r/d=0.25, resulting in g=8. Maximizing the efficiency η with respect to the remaining undetermined parameters u_{lw} and u_{uw} , by setting $\partial \eta/\partial u_{lw}=\partial \eta/\partial u_{uw}=0$, may be shown that the maximum efficiency for this design is attained by taking the belt velocities

$$u_{uw}/U_B = (16 + \tilde{d})F$$
 and $u_{lw}/U_B = \tilde{d}F$ where $\tilde{d} = \frac{d}{\delta}$, $F = \frac{32 + 3\tilde{d} - 2\sqrt{64 + 6\tilde{d}}}{256 + 56\tilde{d} + 3\tilde{d}^2}$.

The variation of the efficiency of this configuration with respect to the remaining parameter, the normalized depth of the water-filled cavity, d/δ , is shown in Figure 15, along with the efficiency of the configurations discussed in the previous two sections.

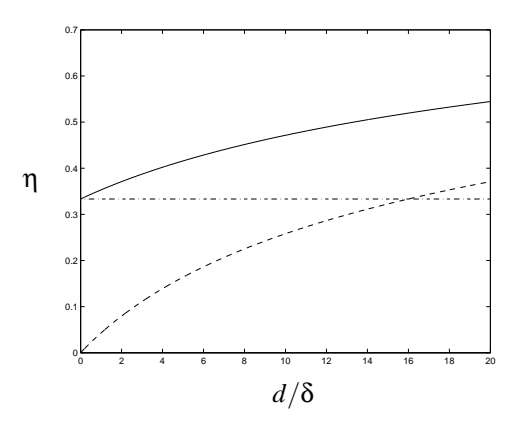


Figure 15: Efficiency of configuration #1 (dashed), configuration #2 (dot-dashed), and onfiguration #3 (solid) for extraction of power from the channel flow using moving-belt mechanisms on the wall, assuming the optimal belt speeds are used in all cases.

2.4.4 Power addition

The three configurations discussed above in the context of power extraction from the flow (for example, for the generation of electricity) may easily be adapted to the problem of the addition of power to the flow (to pump the fluid) simply by driving the rollers with motors rather than extracting energy with generators. The same formulae for $\mathcal{P}_{\text{belt}}$ and $\mathcal{P}_{\text{flow}}$ as considered in the previous sections are still valid, but the belts are now driven to a higher velocity in order to add energy to the flow system. The formulae for computing the efficiency in this power addition problem is given by the reciprocal of formulae (9), (10), and (12) used in the power extraction problems discussed above, that is,

$$\eta = rac{arPliestartantom{P_{
m flow}}}{arPliestartantom{P_{
m belt}}}.$$

For configuration #1, the efficiency in the power addition problem is plotted in Figure 16 as a function of $u_w/U_B > 1$ for several values of $d/\delta > 0$, again taking r/d = 0.25. As in the power extraction problem, it is seen that large values of d/δ are required to achieve over 30% efficiency in this design. It follows in this case that the maximum efficiency for a given cavity depth is given by $u_w/U_\infty = 1 + \sqrt{2g}/\sqrt{2g + 3d/\delta}$, as marked by the asterisks in Figure 16.

For configuration #2, the efficiency of the power addition is maximized by taking $u_w = 3U_B$, for which we again obtain $\eta_{\text{max}} = 1/3$.

For configuration #3, the efficiency of the power addition is maximized by taking

$$u_{uw}/U_B = (16 + \tilde{d})F$$
 and $u_{lw}/U_B = \tilde{d}F$ where $\tilde{d} = \frac{d}{\delta}$, $F = \frac{32 + 3\tilde{d} + 2\sqrt{64 + 6\tilde{d}}}{256 + 56\tilde{d} + 3\tilde{d}^2}$.

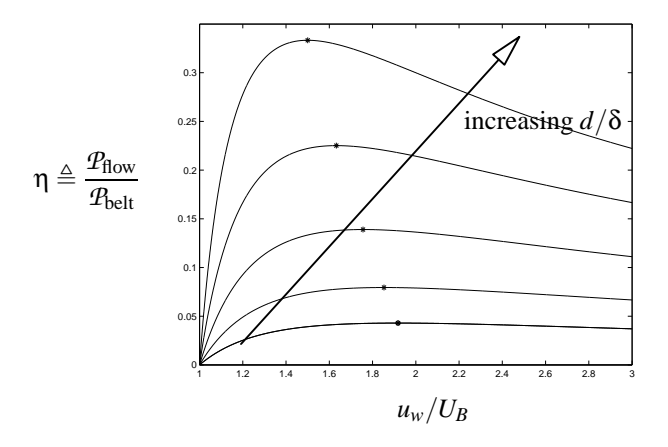


Figure 16: Efficiency of configuration #1 for power addition to a channel flow with the moving-belt mechanism as a function of u_w/U_B for $d/\delta = 1, 2, 4, 8, 16$ with r/d = 0.25.

Note that the belt velocities selected to maximize efficiency in the power addition application are completely different from the belt velocities selected to maximize efficiency in the power extraction application (compare, e.g., Figure 16 and Figure 12). Remarkably, however, the variation of the maximum efficiency with respect to d/δ for the three configurations in the power addition application is *exactly* the same as the variation of the maximum efficiency with respect to d/δ in the power extraction application, as shown previously in Figure 15.

3 Developing laminar boundary-layer flow

Contrary to the channel-flow application, the moving-belt mechanism has very significant engineering benefits in terms of drag reduction and stability enhancement when applied to a boundary layer. In this setting, the location of the belt is beneficial for demarking the edge of the boundary layer, preventing the instabilities which might otherwise arise in an open-cavity flow system (Gharib [49]; Rowley, Colonius, & Basu [50]). As shown in the experiments of Koenig & Roshko [51] and Gharib & Roshko [52], it is possible (in the laboratory setting) to use open cavities to obtain significant drag reduction; however, the instabilites that often arise in such open-cavity flows can often lead to early transition to turbulence and a substantial drag *increase* if the external flow characteristics are not correct. Putting a moving belt at the cavity/boundary-layer interface is an effective way of preventing such instabilities from forming.

As with the channel flow, the moving-belt mechanism allows the drag of the boundary-layer flow to be reduced significantly below that of the flow past a solid wall. In addition, the displacement Reynolds number of the developing boundary layer grows much more slowly when the moving belt is present, so boundary-layer instability and transition to turbulence can be substantially delayed. Since laminar boundary layers have much lower drag than turbulent boundary layers, the transition delay achieved by such a strategy might have a very significant effect on the total drag of the boundary layer.

3.1 Development of boundary-layer profile with moving-belt mechanism

We now repeat the analysis of the previous section, replacing the channel flow in the domain Ω with a laminar boundary layer, as depicted in Figure 17. Starting from the boundary-layer approximation

$$u\frac{\partial u}{\partial x} + v\frac{\partial u}{\partial y} = v\frac{\partial^2 u}{\partial y^2}$$

$$\frac{\partial u}{\partial x} + \frac{\partial v}{\partial y} = 0$$
with
$$\begin{cases} u = U_{\infty}, & v = 0 & \text{at } x = 0, \\ u = u_w(x), & v = 0 & \text{at } y = 0, \\ u \to U_{\infty} & \text{as } y \to \infty, \end{cases}$$

governing the flow in the domain $\{x, y | x > 0, y > 0\}$, where u_w is the velocity of the moving belt in the x-direction and U_{∞} is the velocity of the free stream, and introducing the streamfunction ψ such that

$$u = \frac{\partial \Psi}{\partial y}$$
 and $v = -\frac{\partial \Psi}{\partial x}$, (13)

the continuity equation is satisfied immediately and the momentum equation may be written as

$$\frac{\partial \psi}{\partial y} \frac{\partial^2 \psi}{\partial x \partial y} - \frac{\partial \psi}{\partial x} \frac{\partial^2 \psi}{\partial y^2} = v \frac{\partial^3 \psi}{\partial y^3} \quad \text{with} \quad
\begin{cases}
\psi = U_{\infty} y, & \frac{\partial \psi}{\partial x} = 0 & \text{at } x = 0, \\
\psi = 0, & \frac{\partial \psi}{\partial y} = u_w(x) & \text{at } y = 0, \\
\frac{\partial \psi}{\partial y} \to U_{\infty} & \text{as } y \to \infty.
\end{cases} \tag{14}$$

Note that this system is singular (and, in fact, the approximations leading to it not valid) in the vicinity of the origin x=y=0 but may, with care, be integrated past this singularity. Normalizing by a characteristic length L (for example, the total length of the boundary layer under consideration) and scaling with the Reynolds number $Re_L \triangleq LU_{\infty}/v$ based on L and the characteristic velocity U_{∞} (the free-stream velocity), we now define the dimensionless coordinates ξ and η and a rescaling of the streamfunction, f, such that

$$\xi = \frac{1}{L}x, \qquad \eta = \frac{\sqrt{Re_L}}{L\zeta(\xi)}y, \qquad \text{and} \qquad f = \frac{\sqrt{Re_L}}{LU_{\infty}\zeta(\xi)}\psi(x,y),$$

where $\zeta(\xi)$ is some scaling function which is, as yet, unspecified. To facilitate the analysis (though not strictly necessary in the implementation), we will seek to distribute the cavity depth d in the streamwise coordinate x in such a way as to provide similarity solutions of the boundary-layer profile in which the rescaled streamfunction f is a function of the dimensionless coordinate η only, i.e., $f = f(\eta)$. Such similarity solutions help us to identify and understand the advantages and tradeoffs involved with this strategy for controlling the development of the boundary layer, even though the discrete nature of the implementation (i.e., implementation with a finite number of moving-belt mechanisms) precludes precise realization of such a configuration in practice.

Applying the above definitions and denoting $\zeta' = d\zeta/d\xi$, $f' = df/d\eta$, $f'' = d^2f/d\eta^2$, and $f''' = d^3f/d\eta^3$, we have

$$\frac{\partial \Psi}{\partial x} = \frac{\partial \Psi}{\partial \xi} \frac{\partial \xi}{\partial x} + \frac{\partial \Psi}{\partial \eta} \frac{\partial \eta}{\partial x} = \frac{U_{\infty} \zeta'}{\sqrt{Re_L}} f - \frac{L U_{\infty} \zeta' \eta}{\sqrt{Re_L}} f', \tag{15a}$$

$$\frac{\partial \Psi}{\partial y} = \frac{\partial \Psi}{\partial \eta} \frac{\partial \eta}{\partial y} = U_{\infty} f', \tag{15b}$$

$$\frac{\partial^2 \Psi}{\partial x \partial y} = \frac{\partial U_{\infty} f'}{\partial x} = \frac{\partial U_{\infty} f'}{\partial \eta} \frac{\partial \eta}{\partial x} = -\frac{U_{\infty} \zeta' \eta}{\zeta} f'', \tag{15c}$$

$$\frac{\partial^2 \Psi}{\partial y^2} = \frac{\partial U_{\infty} f'}{\partial y} = \frac{\partial U_{\infty} f'}{\partial \eta} \frac{\partial \eta}{\partial y} = \frac{U_{\infty} \sqrt{Re_L}}{L\zeta} f'', \tag{15d}$$

$$\frac{\partial^{3} \Psi}{\partial y^{3}} = \frac{\partial}{\partial y} \left(\frac{U_{\infty} \sqrt{Re_{L}}}{L \zeta} f'' \right) = \frac{\partial}{\partial \eta} \left(\frac{U_{\infty} \sqrt{Re_{L}}}{L \zeta} f'' \right) \frac{\partial \eta}{\partial y} = \frac{U_{\infty} Re_{L}}{L^{2} \zeta^{2}} f'''. \tag{15e}$$

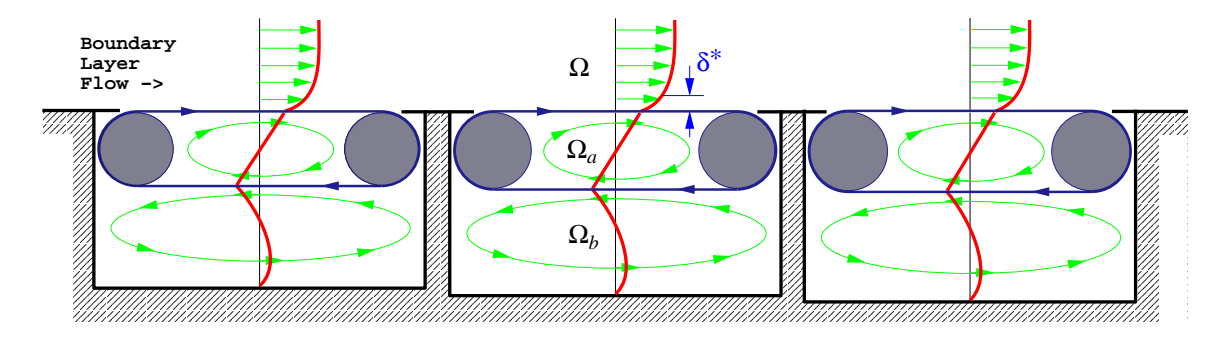


Figure 17: Moving-belt mechanism applied to boundary-layer flow. Note that, when controlling a developing boundary layer, the cavity depths may be designed to increase with the square root of the distance downstream, $d = 2r + h \propto \sqrt{x}$, thereby leading to a discrete approximation of the similarity solution derived in the text. Note that, in the implementation, the wall between adjacent moving-belt mechanisms is unnecessary, but might be beneficial in terms of structural stiffness in an actual (three-dimensional) physical system. To facilitate the analysis, as in §2, we assume that the length of each individual cavity is much larger than its depth, so that 1D profiles may be used to characterize the flows in Ω_a and Ω_b . Note also that the effects of the (possibly significant) variations of $\partial p/\partial x$ near the beginning and end of the moving belts (due to the sudden change in the wall velocity) are neglected.

Inserting (15a)–(15e) into (14) and applying the definition of Re_L yields

$$f''' + (\zeta \zeta')ff'' = 0. \tag{16}$$

In order for the solution of this equation to be invariant in ξ , the coefficient $\zeta\zeta'$ itself must be invariant in ξ . We thus define

$$\zeta(\xi) \triangleq \sqrt{2\xi}.$$

With this definition, the streamfunction representation of the boundary-layer equations (14) in Ω reduces to Blasius' equation with modified boundary conditions

$$f''' + ff'' = 0 \qquad \text{with} \qquad \begin{cases} f = 0, & f' = u_w/U_\infty & \text{at } \eta = 0\\ f' \to 1 & \text{as } \eta \to \infty. \end{cases}$$
 (17)

[Interestingly, Clauser [53] analyzed certain properties of this "slip-wall" laminar boundary-layer system and proposed it as a first-order model of the outer layer of a turbulent boundary layer.] As in §2.1, assuming the length of each individual cavity is much larger than its depth, we may assume the 1D profiles $u_a = u_w y_a/r$ in Ω_a and $u_b = b y_b - c y_b^2$ in Ω_b . Imposing conditions B, C, and D from §2.1 imparts the constraints

$$\begin{split} \frac{h^2 b}{2} - \frac{h^3 c}{3} &= 0, \\ h b - h^2 c + u_w &= 0, \\ \frac{U_{\infty} \sqrt{Re_L}}{L \zeta(\xi)} f''(0) + b - 2hc - \frac{2u_w}{r} &= 0. \end{split}$$

Applying the definitions of Re_L and $\zeta(\xi)$ and combining these three equations to eliminate b and c leads to

$$\frac{u_w}{U_\infty} = \sqrt{\frac{U_\infty}{2vx}} \left(\frac{4}{h} + \frac{2}{r}\right)^{-1} f''(0),$$

from which we can determine an alternative expression for the inhomogeneous boundary condition at $\eta = 0$ which accounts for the friction effects in the recirculation zones Ω_a and Ω_b :

$$f'(0) - kf''(0) = 0$$
 where $k = \sqrt{\frac{U_{\infty}}{2\nu x}} \left(\frac{4}{h} + \frac{2}{r}\right)^{-1}$.

This is a mixed boundary condition on f. In order to obtain the similarity solutions which we seek, the boundary conditions must be independent of x; that is, we must restrict k to be constant. Noting that d = h + 2r and substituting for h results in

$$k = \frac{d}{2g}\sqrt{\frac{U_{\infty}}{2vx}}$$
 where, as before, $g \triangleq \frac{1}{\left(1 - 2\frac{r}{d}\right)\frac{r}{d}}$. (18)

Thus, similarity solutions are obtained by setting $d = 2kg\sqrt{2\nu x/U_{\infty}}$; note that, for a given value of r/d selected, $d \propto k\sqrt{x}$. With this choice of d, the modified Blasius' problem (17) coupled with the boundary conditions imparted by the moving belt may be rewritten as

$$f''' + ff'' = 0 \qquad \text{with} \qquad \begin{cases} f = 0, & f' - kf'' = 0 \\ f' \to 1 & \text{as } \eta \to \infty. \end{cases}$$
 (19)

The constant k is an adjustable parameter which can be set to meet certain design criteria, such as drag reduction or stability enhancement. Note that the limit $d \to 0$ corresponds to $k \to 0$, which recovers the boundary condition for the classical Blasius equation, f'(0) = 0. Figure 18 depicts several self-similar velocity profiles derived from the solution of this system for various values of k. Note that the displacement thickness δ^* and the dimensionless displacement thickness η^* of a boundary layer are defined such that

$$\delta^*(x) \triangleq \int_0^\infty \frac{U_\infty - u}{U_\infty} dy = \sqrt{\frac{2\nu x}{U_\infty}} \eta^* \qquad \text{where} \qquad \eta^* \triangleq \int_0^\infty \frac{U_\infty - u}{U_\infty} d\eta = \int_0^\infty (1 - f') d\eta, \tag{20}$$

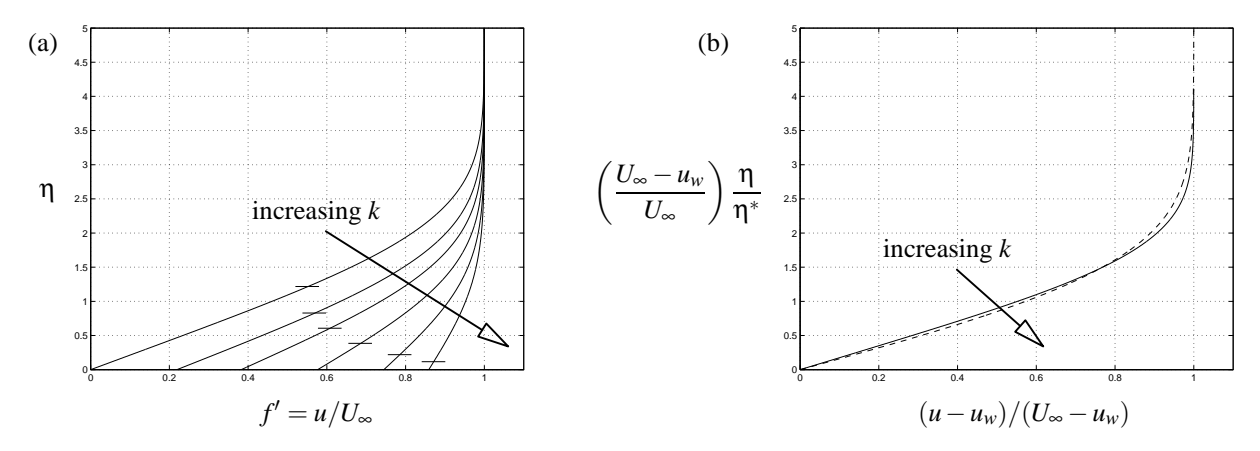


Figure 18: (a) Similarity profiles in the developing boundary layer with the moving-belt mechanism installed, with the cavity depth $d = 2kg\sqrt{2\nu x/U_{\infty}}$ for k = 0, 0.5, 1, 2, 4, and 8, valid for all x. The dimensionless displacement thickness η^* is indicated with a hash mark on each profile; note that η^* is substantially decreased for increased values of k. (b) Similarity profiles scaled in such a way as to reveal their similar shape, plotting only the k = 0 (solid) and k = 8 (dashed) cases for clarity.

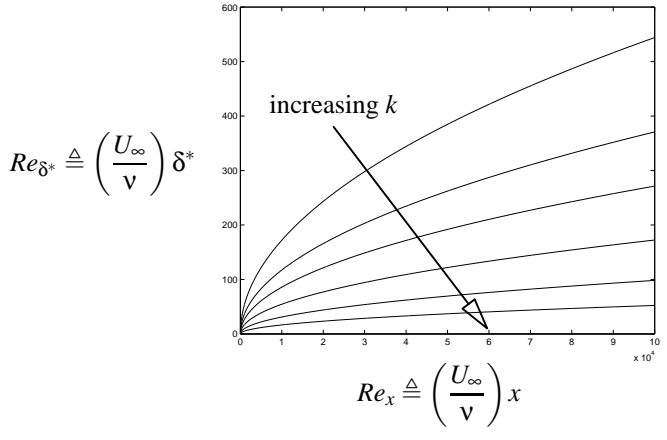


Figure 19: Growth of the displacement Reynolds number in the developing boundary layer for k = 0, 0.5, 1, 2, 4, and 8. Note that the growth rate of δ^* is suppressed substantially when k is increased.

and the displacement Reynolds number Re_{δ^*} of a boundary layer is defined such that

$$Re_{\delta^*} \triangleq \frac{U_{\infty}\delta^*}{v}.$$

As indicated by the hash marks on Figure 18a, the dimensionless displacement thickness of the developing boundary layer is substantially reduced as k is increased. When viewed in the local reference frame of the moving belt and properly rescaled, as shown in Figure 18b, the profiles are seen to be only slightly fuller for increased values of k. [This property was also recognized by Clauser [53].] The reduced growth rate of the displacement Reynolds number Re_{δ^*} in the developing boundary layer for increased values of k, implied by (20) and the values of the dimensionless displacement thickness η^* indicated by the hash marks of Figure 18a, is plotted in Figure 19.

3.2 Accounting for entrainment of the main flow into the lower cavity

Before characterizing the developing boundary layer further, we now consider an alternative configuration of the moving-belt mechanism to that shown in Figure 17. As depicted in Figure 20, we now relax the assumption of zero entrainment of the flow around the ends of the belts.

A calculation of accurate flow profiles in the vicinity of the upstream gap is provided by Tennant, Johnson, & Keaton [54]. In the vicinity of the downstream gap, the flow will be similar to that discussed by Goldstein [19]. The present analysis neglects the exact flow profiles in both of these regions. Rather, in order to facilitate the analysis presented here, we will assume that the gaps at each end of the belt are sufficiently large that there is negligible drop in pressure as the flow moves from Ω into Ω_b around the downstream end of the belt and also that there is negligible

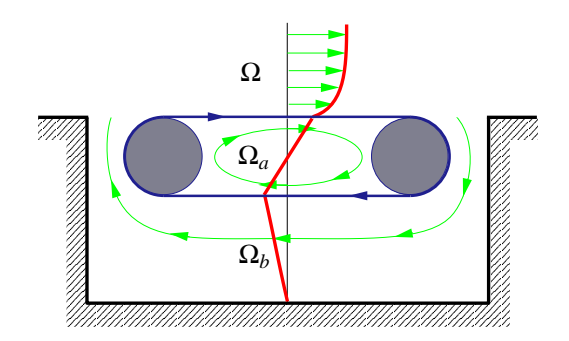


Figure 20: Moving-belt mechanism applied to boundary-layer flow, allowing flow around the ends of the belts. In the implementation, as depicted in Figure 17, several such mechanisms may be installed one after the other, with or without a wall between the adjacent moving-belt mechanisms. The net effect of this strategy is to extract low momentum fluid downstream, thus stabilizing the flow where the boundary layer is thicker, and to reinject this fluid upstream, thus reducing drag where the boundary layer is thin.

drop in pressure as the flow moves from Ω_b back into Ω around the upstream end of the belt. Thus, as we are considering here a zero-pressure-gradient boundary-layer flow in Ω , the pressure gradient in Ω_b in this configuration is approximately zero.

As before, we may assume the 1D profiles $u_a = u_w y_a/r$ in Ω_a and $u_b = b y_b - c y_b^2$ in Ω_b . Imposing the zero-pressure-gradient condition in Ω_b together with conditions C and D from §2.1 imparts the constraints

$$c = 0,$$

$$hb - h^2c + u_w = 0,$$

$$\frac{U_{\infty}\sqrt{Re_L}}{L\zeta(\xi)}f''(0) + b - 2hc - \frac{2u_w}{r} = 0.$$

Applying the definitions of Re_L and $\zeta(\xi)$ and combining these three equations leads to

$$\frac{u_w}{U_\infty} = \sqrt{\frac{U_\infty}{2vx}} \left(\frac{1}{h} + \frac{2}{r}\right)^{-1} f''(0),$$

from which we can determine an alternative boundary condition which accounts for the friction effects in Ω_a and Ω_b :

$$f'(0) - kf''(0) = 0$$
 where now $k = \sqrt{\frac{U_{\infty}}{2\nu x}} \left(\frac{1}{h} + \frac{2}{r}\right)^{-1}$.

Noting that d = h + 2r and substituting for h results in

$$k = \frac{d}{2\tilde{g}} \sqrt{\frac{U_{\infty}}{2\nu x}} \qquad \text{where} \qquad \tilde{g} \triangleq \frac{1 - \frac{3}{2} \frac{r}{d}}{\left(1 - 2\frac{r}{d}\right) \frac{r}{d}}.$$
 (21)

Note that the definition of k in the case with zero pressure gradient in Ω_b , given in (21), is identical to the definition of k in the case with zero mass flux in Ω_b , given in (18), except for the modified definition of g. The two functions g(r/d) and $\tilde{g}(r/d)$ are plotted in Figure 21 for comparison. In the remainder of this paper, we will consider two numerical values for the geometric parameter g: for the case in which Ω_b is zero-net mass flux, with the minimizing r/d selected, we take g=8, and for the case in which Ω_b is zero pressure gradient, with the (different) minimizing r/d selected, we take g=4.5. These two cases represent two extremes: sealing the gaps around the ends of the rollers, or completely opening the gaps around the ends of the rollers. The performance of an actual implementation (neglecting losses due to bearing friction and belt deformation) may be expected to be somewhere in between.

3.3 Drag reduction

The drag force per unit area of the developing boundary-layer profile, from (13) and (15d), is

$$D(x) = \mu \frac{\partial u}{\partial y} \bigg|_{y=0} = \mu \frac{\partial^2 \psi}{\partial y^2} \bigg|_{y=0} = \mu \frac{U_{\infty} \sqrt{Re_L}}{L\zeta(\xi)} f''(0), \tag{22}$$

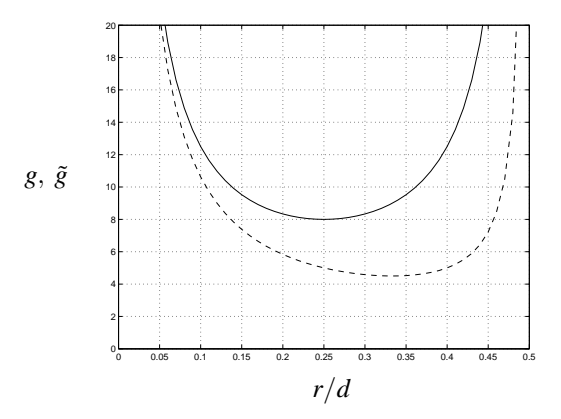


Figure 21: The functions g(r/d) (solid) and $\tilde{g}(r/d)$ (dashed). Note that the minima of the two functions differ by almost a factor of two and occur for different values of r/d: the minimum of g(r/d) is 8 and occurs at r/d = 0.25, whereas the minimum of $\tilde{g}(r/d)$ is 4.5 and occurs at r/d = 1/3.

where f is given by the solution of (19) for some value of k. The drag of the developing boundary-layer profile with no slip boundary conditions, given by the above expression for k = 0, is denoted $D_0(x)$. The resulting expressions for the drag of the developing boundary-layer profile are plotted in Figure 22. For any given values of d, v, x, and U_{∞} , choosing r/d to minimize g:

- A. maximizes k [by (18) or (21)],
- B. thus minimizing the value of f''(0) resulting from the solution of (19) [see, e.g., Figure 18],
- C. thus minimizing the drag D [by (22)].

For this reason, we will refer to the values of r/d that minimize g (see Figure 21) as optimal.

In order to have a substantial beneficial effect, as with the channel flow implementation, the depth of the cavity must be significant with respect to the significant length scales of the bulk flow, in this case taken to be the displacement thickness of the nominal (stationary-wall) Blasius boundary layer, $\delta_0^* = 1.721 \sqrt{vx/U_\infty}$, as shown in Figure 22b. For applications with relatively thin boundary layers, however, this may not be a significant limiting factor in the implementation. In fact, for applications with very thin boundary layers, the fact that the cavity must be many nominal displacement thicknesses deep to have a substantial beneficial effect might sometimes be viewed as an asset rather than a liability, as larger moving-belt mechanisms are easier to manufacture with existing technology.

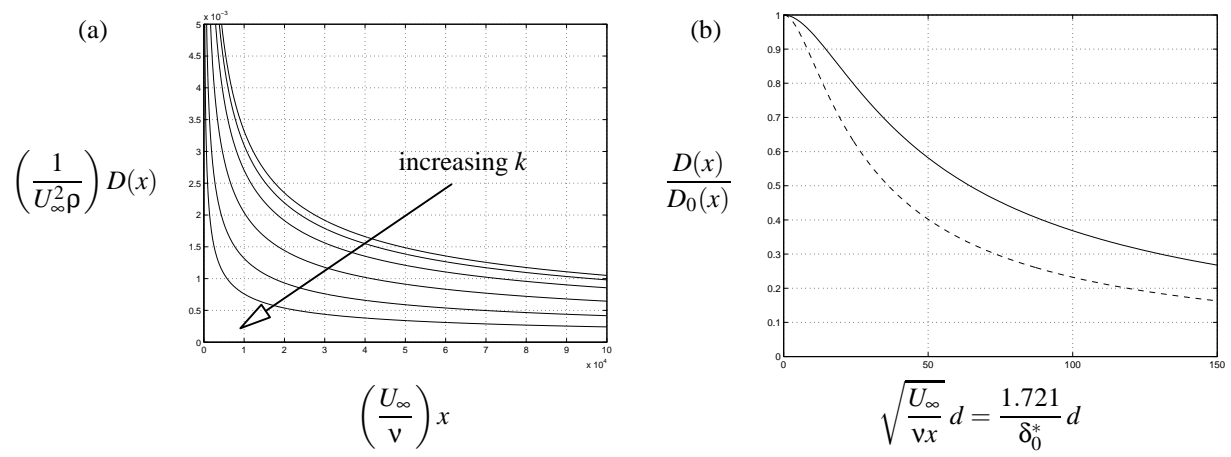


Figure 22: Drag reduction of the developing boundary layer when the passively-driven belt mechanism is installed, taking the cavity depth $d=2kg\sqrt{2vx/U_{\infty}}$. (a) Drag as a function of streamwise distance x for k=0,0.5,1,2,4, and 8. (b) Normalized drag as a function of cavity depth, valid for all x, for the case of zero-net mass flux in Ω_b with r/d=0.25 (solid) and the case of zero pressure gradient in Ω_b with r/d=1/3 (dashed). For a given cavity depth, note that the zero-pressure-gradient configuration is more effective.

3.4 Stability enhancement

Using (locally) the change of variables $\tilde{u} = u - u_w$ introduced in (4) at some particular streamwise location x in the spatially-developing boundary layer, we now define an *effective free-stream velocity* $\tilde{U}_{\infty}(x)$ of

$$\tilde{U}_{\infty}(x) \triangleq U_{\infty} - u_{w}(x),\tag{23}$$

an effective displacement thickness $\tilde{\delta}^*(x)$ of

$$\tilde{\delta}^*(x) \triangleq \int_0^\infty \frac{\tilde{U}_\infty - \tilde{u}}{\tilde{U}_\infty} dy = \frac{U_\infty}{U_\infty - u_w} \int_0^\infty \frac{U_\infty - u}{U_\infty} dy = \frac{U_\infty}{U_\infty - u_w} \delta^*(x), \tag{24}$$

and an effective displacement Reynolds number $\widetilde{Re}_{\delta^*}$ of

$$\widetilde{Re}_{\delta^*} \triangleq \frac{\widetilde{U}_{\infty}\widetilde{\delta}^*}{V} = \frac{U_{\infty}\delta^*}{V} = Re_{\delta^*}.$$
 (25)

We thus see that the appropriately-defined "effective displacement Reynolds number", defined in a reference frame moving with the local belt velocity, is exactly the same as the displacement Reynolds number defined in a stationary reference frame.

For the classical Blasius boundary layer with a stationary wall, the critical value of the displacement Reynolds number for linear instability of the boundary layer is $Re_{\delta^*,crit} = 520$ (Jordinson [55]). In a reference frame moving with the local belt velocity, the similar shapes of the scaled profiles over the wide range of k plotted in Figure 18b indicate that this critical "effective displacement Reynolds number" should be a good indicator of the point of linear instability of the developing boundary layer profile even when the moving-belt mechanism is installed. Indeed, as shown in Figure 23, $Re_{\delta^*,crit}$ is only a relatively weak function of k for $0 \le k \le 8$. Combining the information in Figures 23b and 19, the streamwise location x for linear instability of the laminar boundary layer is seen to be substantially delayed by installation of the moving-belt mechanism, as quantified in Figure 24.

Again, it is well known that bypass mechanisms typically cause transition in boundary layers well before the critical displacement Reynolds number (computed above) is reached. Such bypass mechanisms should be studied closely in the context of the present problem in future work. However, it is reasonable to conclude that the substantial delay in the onset of linear instability of the boundary layer by installation of the moving belt mechanism, shown above, should also be accompanied by a substantial suppression of the related bypass mechanisms.

4 Asymptotic-suction laminar boundary-layer flow

4.1 Asymptotic-suction boundary-layer profile with moving-belt mechanism

We now analyze the boundary layer which eventually develops when uniform suction is applied over the walls by applying distributed suction along the bottom of the cavity in Figure 17 and making the belt porous. Again, we start with the boundary-layer approximation

$$u\frac{\partial u}{\partial x} + v\frac{\partial u}{\partial y} = v\frac{\partial^2 u}{\partial y^2}$$
 with
$$\begin{cases} u = U_{\infty}, & v = 0 \\ u = u_w, & v = -v_w \\ u \to U_{\infty} \end{cases}$$
 at $x = 0$,
$$u = u_w, & v = -v_w \\ u \to U_{\infty} \end{cases}$$
 as $y \to \infty$,

where u_w is the velocity of the moving belt in the x-direction and v_w is the suction velocity through the belt in the negative y-direction. As the velocity profile develops downstream in this case, it eventually approaches an asymptotic limit, at which point u is approximately independent of x, and thus $\frac{\partial u}{\partial x} \approx 0$ and (by continuity and the boundary condition on v) $v \approx -v_w$ throughout the boundary layer. Thus, the boundary-layer system reduces further to

$$v_w \frac{\partial u}{\partial y} - v \frac{\partial^2 u}{\partial y^2} = 0$$
 with
$$\begin{cases} u = u_w, & \text{at } y = 0, \\ u \to U_\infty & \text{as } y \to \infty. \end{cases}$$
 (26)

This second-order ODE is easily solved to obtain the asymptotic velocity profile in Ω :

$$\frac{u(y)}{U_{\infty}} = 1 - \frac{U_{\infty} - u_w}{U_{\infty}} \exp\left(-\frac{v_w}{v}y\right).$$
 (27)

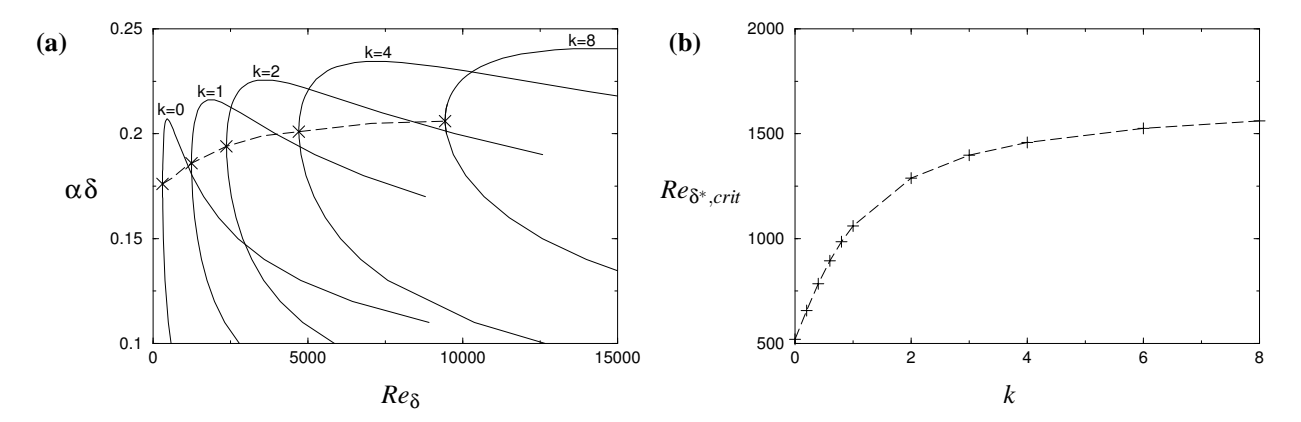


Figure 23: (a) Neutral stability curves (as a function of Reynolds number Re_{δ} and streamwise wavenumber α) of the Orr-Sommerfeld equation for the profiles obtained by numerical solution of the modified Blasius problem (19), such as those depicted in Figure 18a, for various values of k (the classical Blasius case, k=0, is discussed further, e.g., in Figure 3.9a of Schmid & Henningson [46]). As is customary, the length scale δ used to nondimensionalize this plot is defined such that $\delta \triangleq \sqrt{xv/U_{\infty}}$; note that $Re_{\delta} = U_{\infty}\delta/v = \sqrt{Re_x}$. Eigenvalues of the Orr-Sommerfeld problem were determined using the numerical code of P. Cathalifaud (private communication). (b) Critical displacement Reynolds number for linear instability of the solution of the modified Blasius problem, obtained from the critical points marked in Figure 23a and expressed in terms of the Reynolds number based on the displacement thickness δ^* . As k is increased from 0 to 8, the scaled velocity profile becomes slightly fuller (Figure 18b), and thus $Re_{\delta^*,crit}$ increases gradually with k.

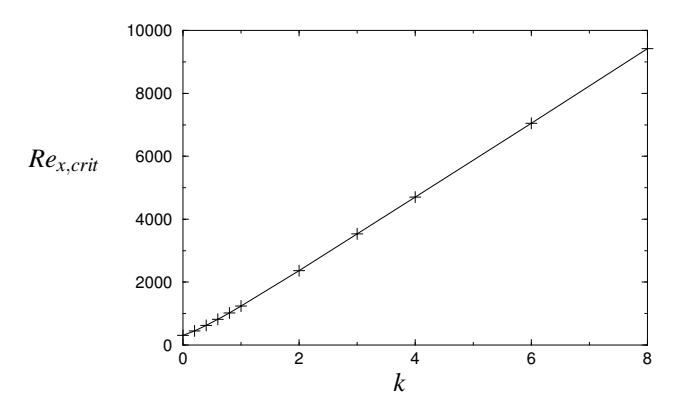


Figure 24: Streamwise location x for linear instability of the developing laminar boundary layer profile as a function of k. Note that the retardation of the streamwise location of linear instability of the boundary layer as k is increased is primarily due to the reduced growth rate of Re_{δ^*} with x in the boundary layer as k is increased (due to the substantial reduction in the momentum loss at the wall when the wall is moving), as indicated in Figure 19, and, to a lesser extent, to the modest increase in $Re_{\delta^*,crit}$ as k is increased (due to the slight change in shape of the scaled velocity profile), as indicated in Figure 23b.

As before, we may assume the 1D profiles $u_a = u_w y_a/r$ in Ω_a and $u_b = b y_b - c y_b^2$ in Ω_b . For the case with zero-net mass flux in Ω_b , imposing conditions B, C, and D from §2.1 imparts the constraints

$$\frac{h^2 b}{2} - \frac{h^3 c}{3} = 0,$$

$$hb - h^2 c + u_w = 0,$$

$$\frac{v_w}{v} (U_\infty - u_w) + b - 2hc - \frac{2u_w}{r} = 0.$$

Combining these three equations to eliminate b and c leads to the belt velocity

$$\frac{u_w}{U_\infty} = \frac{v_w d/\nu}{2g + v_w d/\nu},\tag{28}$$

where we have again applied the definitions d = 2r + h and $g = \left[\left(1 - 2\frac{r}{d}\right)\frac{r}{d}\right]^{-1}$. On the other hand, for the case with zero pressure gradient in Ω_b , imposing the zero pressure gradient condition together with conditions C and D from §2.1 imparts the constraints

$$c = 0,$$

$$hb - h^2c + u_w = 0,$$

$$\frac{v_w}{V}(U_\infty - u_w) + b - 2hc - \frac{2u_w}{r} = 0.$$

Combining these three equations leads to the belt velocity

$$\frac{u_w}{U_\infty} = \frac{v_w d/v}{2\tilde{g} + v_w d/v},\tag{29}$$

where we have again applied the definition $\tilde{g} = \left[1 - \frac{3}{2} \frac{r}{d}\right] / \left[\left(1 - 2\frac{r}{d}\right) \frac{r}{d}\right]$. Note that, as before, the formulae for the belt velocity (28) and (29) have the same form with different values of g. The velocity profiles which result by combining (27) with (28) or (29) are shown in Figure 25a. Note that, in contrast with the developing boundary layer case depicted in Figure 18, when viewed in the reference frame of the moving belt and properly rescaled, all of the profiles in the asymptotic boundary layer case (Figure 25a) have precisely the same shape. Note that the displacement thickness of the asymptotic boundary layer profile is

$$\delta^* \triangleq \int_0^\infty \frac{U_\infty - u}{U_\infty} dy = \int_0^\infty \frac{U_\infty - u_w}{U_\infty} \exp\left(-\frac{v_w}{v}y\right) dy$$

$$= \left[-\frac{v}{v_w} \frac{U_\infty - u_w}{U_\infty} \exp\left(-\frac{v_w}{v}y\right)\right]_0^\infty = \frac{v}{v_w} \left(1 - \frac{u_w}{U_\infty}\right). \tag{30}$$

The displacement Reynolds number as a function of cavity depth for several values of the suction velocity is shown in Figure 25b.

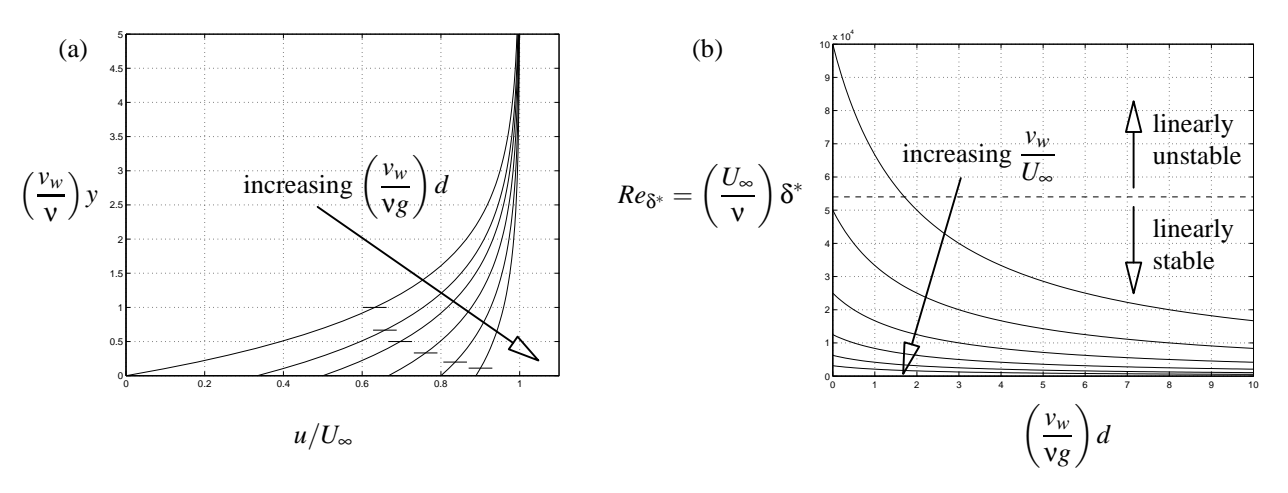


Figure 25: (a) Velocity profiles in the asymptotic boundary layer with suction, with cavity depth d selected such that $v_w d/(vg) = 0$, 1, 2, 4, 8, and 16. The nondimensionalized displacement thickness $v_w \delta^*/v = (1 - u_w/U_\infty)$ [see (30)] is marked on each profile; note that, for a given v_w , the displacement thickness is substantially reduced for increased values of d. (b) Displacement Reynolds number plotted as a function of nondimensionalized cavity depth for $v_w/U_\infty = 0.00001$, 0.00002, 0.00004, 0.00008, 0.00016, and 0.00032. Note that Re_{δ^*} may be reduced by increasing d, by increasing v_w , or both.

4.2 Drag reduction

The drag of the asymptotic boundary-layer profile, determined from (27) and either (28) or (29), is given by

$$D = \mu \frac{\partial u}{\partial y} \bigg|_{v=0} = \mu \frac{v_w U_\infty}{v} \left(1 - \frac{u_w}{U_\infty} \right) = \rho v_w U_\infty \left(\frac{2g}{2g + v_w d/v} \right).$$

The drag of the asymptotic boundary-layer profile with no-slip boundary conditions is $D_0 = \rho v_w U_\infty$. The resulting expressions for the drag of the asymptotic boundary-layer profile are plotted in Figure 26. Note that, as with the developing boundary layer of §3.1, the optimum roller size providing the greatest drag reduction is that which minimizes g, i.e., r/d = 0.25 in the zero-net mass flux case, resulting in g = 8, and r/d = 1/3 in the zero pressure gradient case, resulting in g = 4.5.

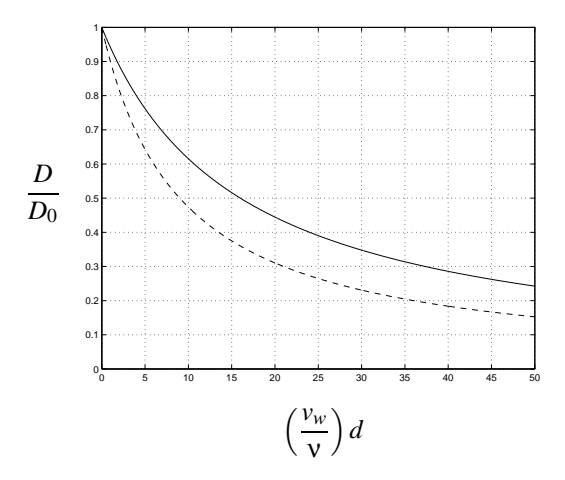


Figure 26: Drag reduction of asymptotic boundary layer with applied suction when the passively-driven belt mechanism is installed. Normalized drag is plotted as a function of cavity depth, valid for all v_w , for the case of zero-net mass flux in Ω_b with r/d = 0.25 (solid) and the case of zero pressure gradient in Ω_b with r/d = 1/3 (dashed). For a given cavity depth, note that the zero-pressure-gradient configuration is more effective.

4.3 Stability enhancement

By the same derivation as (23)-(25), it follows in the present case that the "effective displacement Reynolds number", defined in a reference frame moving with the belt velocity, is exactly the same as the displacement Reynolds number defined in a stationary reference frame. For the classical asymptotic suction profile with a stationary wall, the critical value of the displacement Reynolds number for linear instability is $Re_{\delta^*,crit} = 54,370$ (Hocking [56]). As mentioned previously, when viewed in a reference frame moving with the belt velocity, all of the asymptotic suction profiles have an identical shape. Thus, linear stability of the asymptotic suction profile with the moving-belt mechanism installed may be characterized by the single parameter Re_{δ^*} . As quantified in Figure 25b, the profile may be stabilized by either increasing v_w , increasing d, or both.

Again, bypass mechanisms typically trigger transition well below the critical displacement Reynolds number, so v_w and d should be selected to provide a conservative safety margin below this value if laminar flow is desired.

4.4 Reduced suction requirement for maintaining target Re_{δ^*}

As seen in Figure 25b, in order to design a laminar-flow asymptotic boundary layer via a combination of suction and the moving-belt mechanism, one may select v_w and d such that Re_{δ^*} is sufficiently low to insure laminar flow. We now discuss further how the tradeoff between v_w and d may be performed in order to obtain the target value of Re_{δ^*} .

If the belt is not moving $(u_w = 0)$, the suction velocity required to achieve a target displacement Reynolds number of Re_{δ^*} may be determined by first computing the target displacement thickness $\delta^* = Re_{\delta^*} v/U_{\infty}$, then computing the required suction velocity from (30):

$$v_{w,0} = \frac{\mathsf{v}}{\delta^*}.\tag{31}$$

If the cavity depth is nonzero and the belt is moving $(u_w \neq 0)$, the displacement thickness may be written, using (30) and (28), as

$$\delta^* = \frac{\mathsf{v}}{\mathsf{v}_w} \left(\frac{2\mathsf{g}}{2\mathsf{g} + \mathsf{v}_w d/\mathsf{v}} \right).$$

In order to obtain the target displacement thickness δ^* , the suction velocity required is found by taking the positive

root of the resulting quadratic equation for v_w , that is

$$v_w = \frac{vg}{d} \left(-1 + \sqrt{1 + \frac{2}{g} \frac{d}{\delta^*}} \right). \tag{32}$$

Thus, the reduction in required suction that follows from allowing the belt to move can be expressed, using (31) and (32), as

$$\frac{v_w}{v_{w,0}} \triangleq g \frac{\delta^*}{d} \left(-1 + \sqrt{1 + \frac{2}{g} \frac{d}{\delta^*}} \right).$$

This expression reveals that the suction reduction ratio $v_w/v_{w,0}$ is a function of g and d/δ^* only. This function is plotted in Figure 27.

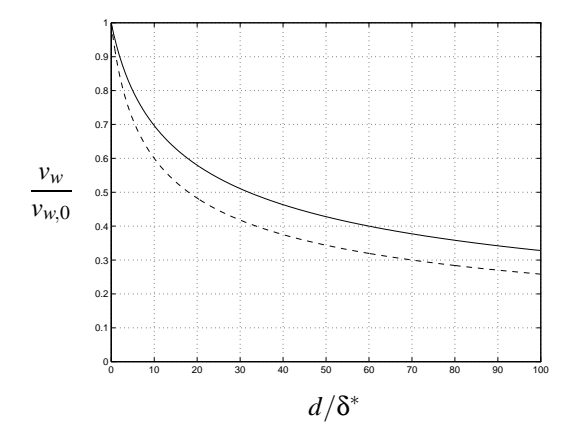


Figure 27: Reduced suction requirement for maintaining a target Re_{δ^*} when the passively-driven belt mechanism is installed, plotted as a function of nondimensionalized cavity depth, for the case of zero-net mass flux in Ω_b with r/d = 0.25 (solid) and the case of zero pressure gradient in Ω_b with r/d = 1/3 (dashed). This curve is valid for all δ^* .

4.5 Reduced suction requirement for maintaining target Re_{θ}

In the prevention of particular mechanisms for bypass transition, it is sometimes of interest to design for a specific target Reynolds number based on momentum thickness, Re_{θ} , rather than a target Reynolds number based on displacement thickness, Re_{δ^*} . As shown in this section, this is also a straightforward problem, and can be accomplished by another tradeoff between the suction v_w and the cavity depth d.

The momentum thickness is

$$\begin{split} \theta &\triangleq \int\limits_0^\infty \frac{u}{U_\infty} \frac{(U_\infty - u)}{U_\infty} dy = \int\limits_0^\infty \left(1 - \frac{U_\infty - u_w}{U_\infty} \exp\left(- \frac{v_w}{v} y \right) \right) \left(\frac{U_\infty - u_w}{U_\infty} \exp\left(- \frac{v_w}{v} y \right) \right) dy \\ &= \left[- \frac{v}{v_w} \frac{U_\infty - u_w}{U_\infty} \exp\left(- \frac{v_w}{v} y \right) + \frac{v}{2v_w} \left(\frac{U_\infty - u_w}{U_\infty} \right)^2 \exp\left(- 2 \frac{v_w}{v} y \right) \right]_0^\infty \\ &= \frac{v}{v_w} \left(1 - \frac{u_w}{U_\infty} \right) \left(1 - \frac{1}{2} \left(1 - \frac{u_w}{U_\infty} \right) \right). \end{split}$$

If the belt is not moving $(u_w = 0)$, the suction velocity required to achieve a momentum thickness of θ is

$$v_{w,0} = \frac{v}{2\theta}.\tag{33}$$

If the cavity depth is nonzero and the belt is moving $(u_w \neq 0)$, the momentum thickness may be written, using (28), as

$$\theta = \frac{v}{v_w} \left(\frac{2g}{2g + v_w d/v} \right) \left(\frac{g + v_w d/v}{2g + v_w d/v} \right).$$

Thus, in order to obtain a prescribed momentum thickness, we need to solve the following third-order algebraic equation for the suction, v_w

$$v_w^3 + \frac{4vg}{d}v_w^2 + \left(\left(\frac{2vg}{d}\right)^2 - 2\frac{v^2g}{d\theta}\right)v_w - \frac{v}{2\theta}\left(\frac{2vg}{d}\right)^2 = 0.$$
 (34)

Defining

$$\phi = \frac{2vg}{d}$$
, $r = 2\phi$, $s = \phi^2 - \phi \frac{v}{\theta}$, and $t = -\frac{\phi^2 v}{2\theta}$,

equation (34) takes the form

$$v_w^3 + rv_w^2 + sv_w + t = 0.$$

Defining $x = v_w + r/3 = v_w + 2\phi/3$ yields

$$x^{3} + px + q = 0$$
 where $p = s - \frac{r^{2}}{3} = -\frac{\phi^{2}}{3} - \frac{v\phi}{\theta}$, $q = \frac{2r^{3}}{27} - \frac{rs}{3} + t = \frac{\phi^{2}(9v - 4\phi\theta)}{54\theta}$. (35)

Note that, since $\phi > 0$, v > 0, and $\theta > 0$, it follows that

$$(p/3)^3 + (q/2)^2 = -\frac{v\phi^3 \left(16v^2 + 13v\phi\theta + 8\phi^2\theta^2\right)}{432\theta^3} < 0.$$

The (real) roots of the cubic equation (35) are therefore given by the analytic formulae of *casus irreducibilis* (see, e.g., Gellert *et al.* [57]). In terms of v_w , the only positive real root, for any cavity depth d > 0, is given by

$$v_w = 2\sqrt[3]{m}\cos\left(\frac{\varphi}{3}\right) - \frac{2}{3}\phi$$
 where $m = \sqrt{-\left(\frac{p}{3}\right)^3}$, $\cos\varphi = -\frac{q}{2m}$. (36)

Thus, the reduction in suction that follows from allowing the belt to move can be expressed, using (33) and (36), as

$$\frac{v_w}{v_{w,0}} = \frac{2\sqrt[3]{m}\cos(\phi/3) - 2\phi/3}{v/(2\theta)}$$

$$= \frac{4\sqrt{2g}}{3}\frac{\theta}{d}\sqrt{\left(3\frac{d}{\theta} + 2g\right)}\cos\left(\frac{1}{3}\arccos\left(\frac{\sqrt{g}\left(-9\frac{d}{\theta} + 8g\right)}{\left(6\frac{d}{\theta} + 4g\right)^{3/2}}\right)\right) - \frac{8g}{3}\frac{\theta}{d}}.$$
(37)

This expression reveals that the suction reduction ratio $v_w/v_{w,0}$ is a function of g and d/θ only. This function is plotted in Figure 28.

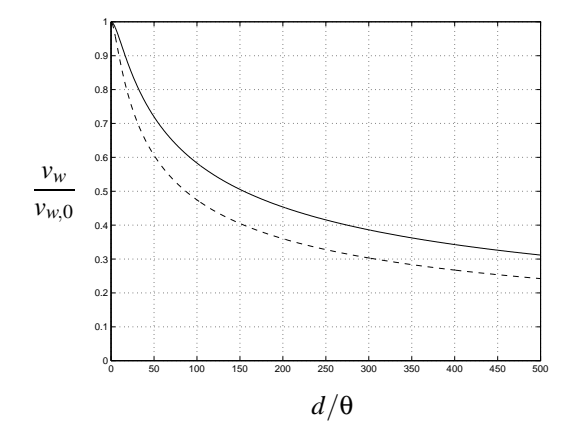


Figure 28: Reduced suction requirement for maintaining a target Re_{θ} when the passively-driven belt mechanism is installed, plotted as a function of normalized cavity depth d/θ , for the case of zero-net mass flux in Ω_b with r/d = 0.25 (solid) and the case of zero pressure gradient in Ω_b with r/d = 1/3 (dashed). This curve is valid for all θ .

5 Future work: a variety of active control applications

The previous three sections have been devoted to the quantification of the drag-reduction and stability-enhancement properties of the passively driven moving-belt mechanism when applied to simple laminar flows for which analytic or similarity solutions are possible. Such idealized systems might never be precisely realized in practice due to the discrete nature of any implementation on a finite number of moving-belt mechanisms. However, these solutions do provide insight as to the essential tradeoffs (with cavity depth, roller size, suction velocity, and gap width) and scaling (with Reynolds number) inherent with the passively-driven moving-belt mechanism for the purposes of drag reduction and stability enhancement in more practical settings, such as airfoils and ship hulls.

When one applies a motor to the rollers, a wide range of promising applications for the moving belt mechanism arise. We now summarize briefly several of these applications; detailed analysis of these designs is deferred to future work. As we will now consider schemes which actively apply energy to the flow via the belt mechanism, we will refer to the following schemes as "active control". However, the decision of what belt velocity to use will be based at most on bulk flow quantities, so these flow control strategies are essentially characterized as "open loop". We mention again that the designs proposed appear to be most promising for UAV/UUV applications in which viscous effects dominant and the efficiency of traditional higher-Reynolds number designs is degraded.

5.1 Detection and prevention of separation / stall

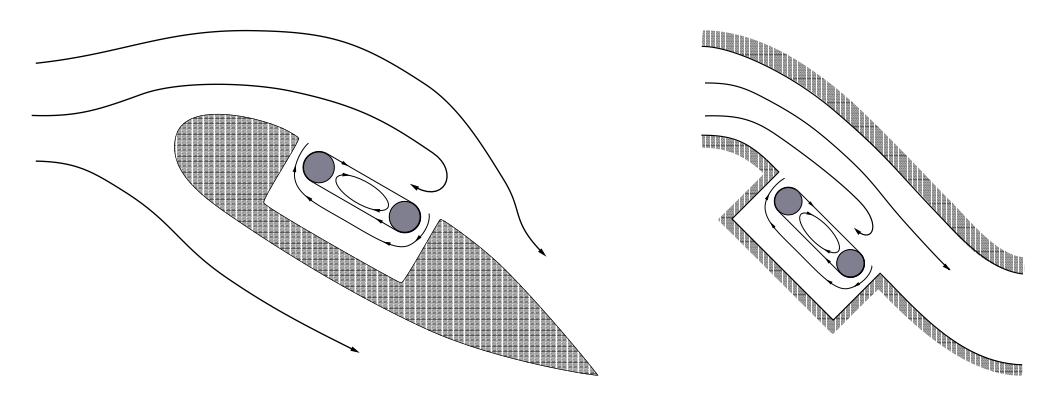


Figure 29: Moving-belt mechanism applied near the separation point of an airfoil (left, similar to Favre's design in §1) and a curved duct such as a serpentine engine inlet (right). In both of the cartoons shown, the moving-belt mechanism is enlarged for clarity of the presentation; in an actual implementation, the mechanism used could be much smaller.

Certain aeronautical subsystems, such as airfoils at high angle of attack and the curved ducts commonly used for stealth engine inlets (see Figure 29), are particularly prone to separation at critical flight conditions. By installing a moving-belt mechanism near the separation point in such systems, and mounting a generator to one of the rollers of this mechanism, one can estimate the average friction of the flow over the belt. As separation of the flow is approached, this friction decreases and eventually changes sign. Thus, by monitoring the output of the generator, one can detect the onset of separation and stall. When its onset is detected, separation can easily be prevented in such a system simply by applying power to the generator, driving it as an electric motor. This accelerates the belt in the streamwise direction, thereby re-energizing the flow in the streamwise direction near the wall.

5.2 Thrust production

5.2.1 Airfoils

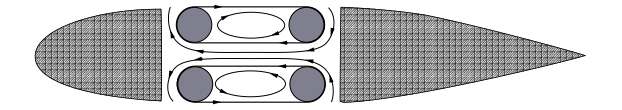


Figure 30: Symmetric configuration of belts on an airfoil.

Installation of motor-driven moving-belt mechanisms on the upper and lower surfaces of an airfoil, as depicted in Figure 30, and driving the belts of these mechanisms faster than the free-stream velocity provides the opportunity

for the efficient production of thrust. Note that, by removing the wall between the upper and lower driven-belt mechanisms, the losses in this region are eliminated. If the speeds of the two belts are different, the Couette flow in the region between the belts simply extracts power from one belt and applies it to the other.

Note also that, as the driven-belt mechanism accelerates the flow near the wall, the skin friction on the airfoil aft of the belt mechanism is actually increased with this approach. In order to mitigate this effect, the belt mechanisms may be extended as close as practicable to the trailing edge of the airfoil.

In addition, as the momentum of the fluid near the belt is higher than that of the free stream in this application, the gap after the downstream roller is not useful for extracting low-momentum fluid from the flow. Thus, the gaps at the ends of both rollers, as well as the gap between return portion of the belts, should be kept fairly small in this application.

5.2.2 Underwater applications

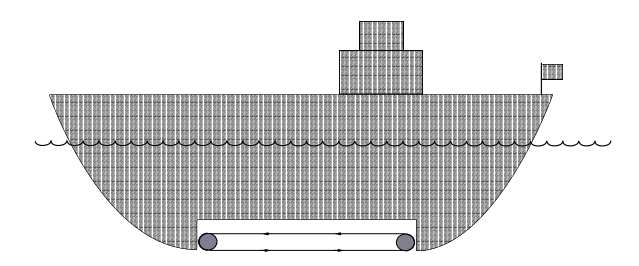


Figure 31: Underwater application for efficient and quiet production of thrust.

Installation of a driven-belt mechanism on the lower surface of an underwater vehicle for the efficient and quiet production of thrust is also straightforward, as indicated in Figure 31. In this application, the cavity containing the driven-belt mechanism may be filled with pressurized air (at the pressure of the water at the bottom of the hull). As the viscosity of air is only about 1% that of water, this is an effective strategy to minimize the losses due to the recirculating fluid within the driven-belt mechanism. The buoyancy of the air acts to trap the air within the cavity, so only a small amount of air needs to be applied to refill the cavity as the system operates in order to make up for any losses due to the pitching and rocking of the vessel. Note that the low viscosity of air (as compared with that of water) is the same principle that gives hydrofoils their efficiency, though the present configuration allows efficient operation at much lower power settings than that required by hydrofoils, as the pocket of air on which the ship glides is confined by the cavity in the bottom of the hull. Note also that the vessel may be stopped by driving the belt in the backwards direction, and for certain applications one might even consider a symmetric hull design to create a vessel which may travel efficiently in either direction. One of the primary challenges of this application might be the production of an elastic, durable belt for underwater use, as discussed further in §5.5. Note that, for the purpose of just attaining drag reduction (rather than thrust production), one may dispense with the belt mechanism entirely, and simply glide on the pocket of air confined (by its buoyancy) within the cavity in the bottom of the hull. This idea is loosely related to the high system efficiencies attainable by supercavitating underwater projectiles which travel completely immersed in their own gas pocket (Ashley [58]), but may be realized in low-speed applications.

5.3 Lift enhancement

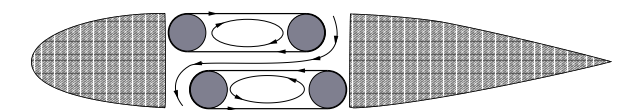


Figure 32: Asymmetric configuration of input and output to the gap between the belts leads to an increased pressure below the wing and a decreased pressure above the wing, thereby producing lift.

By driving the belts of Figure 30 at different speeds, the flow in the boundary layer is made to move more quickly over one side of the airfoil than the other, and thus a difference in pressure between the upper and lower surfaces results, creating lift via the aforementioned "Magnus effect". However, for applications with thin boundary layers, the resulting pressure differential between the upper and lower surfaces is only slight, as the acceleration of the fluid

due to the moving-belt mechanism is confined to the boundary layer, and thus may be accounted for in terms of the exterior flow simply by a small change in the boundary-layer thickness.

In order to achieve a more substantial enhancement of lift, it is possible to arrange the input and output of the gap between the belts asymmetrically, as shown in Figure 32. This design not only creates lift, by decreasing the pressure near the sink on the suction side of the airfoil and increasing the pressure near the source on the pressure side of the airfoil, but it also inhibits separation, by extracting low-momentum fluid near the separation point on the suction side of the airfoil.

As discussed in §1.1, a closely-related technique to enhance the lift of an airfoil is to embed a rotating circular cylinder at the leading edge, trailing edge, or mid-chord on an airfoil. Such a mechanism can alter the circulation around the airfoil significantly, and has proven to be quite effective in both aeronautical (Tennant, Johnson, & Krothapalli [59]; Modi *et al.* [60]) and maritime (Brooks [20]; Steele & Harding [17]) applications.

5.4 Attitude control

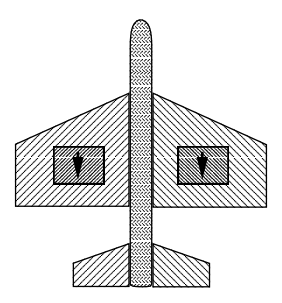


Figure 33: Plan view of a UAV/UUV with moving-belt mechanism installed on each wing for a combination of thrust, lift enhancement, and attitude control. Note in this view that the rollers at the leading and trailing edges of each belt are themselves appropriately positioned to bear (axially) some of the structural load of the wing itself.

Consider a small UAV or UUV with a moving-belt mechanism installed on the top and bottom surfaces of both the left and right wings, as shown in section view in Figure 30 and in plan view in Figure 33. For simplicity of the present description, consider first just one belt in each of these locations, for a total of four belt mechanisms. Let us denote them as LB, LT, RB, and RT for the left-bottom, left-top, right-bottom, and right-top respectively. Note that all four moving-belt mechanisms may be driven independently (with motors) to the velocities u_{LB} , u_{LT} , u_{RB} , and u_{RT} in order to propel the airplane in flight, providing thrust as discussed in §5.2.1 and lift as discussed in §5.3.

Take \bar{u}_{LB} , \bar{u}_{LT} , \bar{u}_{RB} , and \bar{u}_{RT} as the velocity of the belts when the airplane is trimmed in straight-and-level flight. Attitude control of the aircraft in both roll and yaw is then straightforward simply by applying differential corrections to the velocities of the four belts:

```
A. to roll, take: u_{LB} = \bar{u}_{LB} + r, u_{LT} = \bar{u}_{LT} - r, u_{RB} = \bar{u}_{RB} - r, and u_{RT} = \bar{u}_{RT} + r, B. to yaw, take: u_{LB} = \bar{u}_{LB} + y, u_{LT} = \bar{u}_{LT} + y, u_{RB} = \bar{u}_{RB} - y, and u_{RT} = \bar{u}_{RT} - y.
```

In the roll mode, the differential corrections to the belt velocities give one wing more lift than the other, and in the yaw mode, the differential corrections to the belt velocities give one wing more thrust than the other. The control authority via this strategy for both yaw and roll control should be quite adequate, as the moment arm through which the torques are applied are large around these axes. The design discussed here does not address pitch control, and thus a conventional horizontal stabilizer might need to be retained.

5.5 Implementation issues

The analyses in §2, 3, & 4, and to a large extent the brief discussion of active control strategies in §5, bypass the description of several significant implementation issues. We mention briefly only a few of these practical matters here.

The selection of an appropriate material for the belt is probably the primary practical challenge in the realization of this system in an actual engineering design. The operating fluid (air or water), the corrosiveness of the environment (such as seawater), the load the belt is expected to experience, and the speed at which the belt must turn in a particular implementation will all affect the selection of the appropriate belt material. Reinforced rubber and spring steel are two possible alternatives. It is important to note that, in the automotive industry, there has been extensive development of belt technology for high-load applications, such as the van Doorne type continuously-variable transmissions (Hendriks,

ter Heegde, & van Prooijen [61]), one of which was implemented in the Williams Formula 1 racecar in 1993. Edge guides and/or a slight convexity of the rollers are also required to keep the belt running straight; Bechert, Hage, & Brusek [27] discuss further some of the practical challenges related to this issue. Also, for the driven applications, the belt must have sufficient traction against the rollers that it does not slip. Brown [3] discusses some of the important issues related to the balancing of the rollers.

A significant implementation issue limiting the practicality of suction-based laminar flow control (LFC) wing designs is the clogging of suction holes with debris such as dirt and insects (for a thorough review of early LFC efforts, see Lachmann [62]). Combining suction with the moving-belt mechanism offers a possibility for self-cleaning to mitigate this effect. Recalling that the belt is propelled by the drag force of the overlying flow, debris from the external environment which impacts the belt is likely to be flung off near the downstream roller. In addition, if there is no wall between adjacent moving-belt mechanisms, the motion of the upstream roller on the next moving-belt mechanism will tend to deflect debris out of the plenum. Even if some debris does manage to get into the plenum, if the space between the rollers is made smaller than the diameter of the suction hoses, the debris which can enter the plenum will be small, and the applied suction should keep the plenum clean without clogging. Suction also keeps uniform downward pressure on belt, preventing the possible flapping of the belt that might otherwise disturb the flow near the belt and incite transition to turbulence.

6 Conclusions

This article analyzed the efficiency of a simple moving-belt mechanism for laminar boundary-layer control in a variety of practical applications, including drag reduction and transition delay. Particular attention was paid to the losses due to the recirculating viscous fluid within the moving-belt mechanism, leading to the conclusion that these recirculation zones must be made sufficiently large for the design to be energetically efficient. This is in contrast to several mechanisms tested in previous work and reviewed in §1; of those reviewed, only the one by Bechert, Hage, & Brusek [27] employed relatively large recirculation zones for an energetically-efficient design.

Initial analysis of the application of this mechanism to channel flows (§2) led to the proposal of a new strategy for power extraction or addition in viscous-dominated flows via the acceleration of the flow into a narrow channel (via a converging nozzle) and subsequent extraction or addition of power via moving-belt mechanisms mounted in sufficiently-deep cavities in the walls. Filling the upper cavities with air at the appropriate pressure was proposed as a means to improve efficiency. It was found that a large ratio of the cavity depth to the channel width was required for this design to be energetically efficient. However, in viscous-dominated flows in certain niche applications, such as micromachines, a variant of this design might prove to be competitive with more traditional strategies based on turbines.

Analysis of the application of the mechanism to developing boundary layers (§3) revealed that the design can be used effectively in a passive configuration, both to reduce drag and to delay separation. Scaling the cavity depths with the square-root of the distance downstream and approximating the discrete implementation with a continuous representation, a generalization of the Blasius boundary layer was identified. Allowing flow through the gaps at each end of the belt (into the cavity through the downstream gap, and out of the cavity through the upstream gap) was shown to improve the efficiency of the mechanism.

Analysis of the application of the mechanism to a boundary layer with distributed suction (§4) also revealed that the design can be used effectively in a passive configuration, both to reduce drag and to reduce the suction required in order to attain a desired target Reynolds number of the asymptotic-suction profile to maintain laminar flow.

Finally, a variety of practical active control applications for the moving-belt mechanism were proposed for future investigation (§5). Computational and experimental characterization of the practical issues related to these designs is deferred to future work. Other issues which remain to be addressed include the application to turbulent flows, accounting for finite aspect ratios in the cavities Ω_a and Ω_b , and accounting for the various "bypass" paths to transition in the several configurations proposed. Contrary to many feedback strategies for active control of turbulence, the present mechanism might also be quite effective even at high Reynolds numbers when the overlying flow is fully turbulent. In this case, however, the analytical analysis done in the present paper must be supplemented by experiments and/or numerical simulations to quantify the benefits that can be obtained with the moving-belt mechanism.

Acknowledgements

The author is indebted to Dr. Ole Morten Aamo for several engaging discussions regarding the moving-belt mechanism, to Dr. Patricia Cathalifaud for the computation of the neutral stability curves of the modified Blasius boundary layer, and to Prof. Dietrich Bechert for his feedback concerning the implementation difficulties of this design. Sincere

thanks are also given to Prof. Joseph Katz, Prof. Stephane Labbe, Dr. Clark Lee Merriam, Mr. Robert Nelson, and Prof. Erich Truckenbrodt for assistance in obtaining some of the key references.

References

- [1] Tokaty, G.A. (1971) A history and philosophy of fluidmechanics. Foulis % Co., Ltd.
- [2] Alvarez-Calderon, A. (1964) Rotating cylinder flaps of V/STOL aircraft Aircraft Eng. 36, 304-309.
- [3] Brown, D.A. (1964) Peruvians study rotating-cylinder flap *Aviation Week & Space Technology*, Dec. 7, 1964, pp. 70-76. (See also *A.W.&S.T.* Oct. 18, 1971, p. 19, and Dec. 13, 1971, cover.)
- [4] Cichy, D.R., Harris, J.W., & MacKay, J.K. (1972) Flight tests of a rotating cylinder flap on a North American Rockwell YOV-10 aircraft *NASA CR-2135*.
- [5] Magnus, G. (1853) Ueber die Verdichtung der Gase an der Oberflache glatter Korper. *Poggendorfs Annalen der Physik und Chemie* **88** (1), 604-610.
- [6] Swanson, W.M. (1961) The Magnus Effect: a summary of investigations to date. *Journal of Basic Engineering*, **83**, 461-470.
- [7] Flettner, A. (1925) The Flettner roto ship. Engineering, 19, 117-120.
- [8] Flettner, A. (1926) The story of the rotor, from the German Mein Weg zum Rotor. Willhofft.
- [9] Dunn, L. (1973) Merchant Ships of the World 1910-1929 in colour. Blandford Press Ltd, p. 102.
- [10] Leek, B.M. (1997) The German Rotor Ship "Barbara" of 1926, Sea Breezes, the magazine of ships and the sea 71 (616), 288-292.
- [11] Park, J. (1981) The wind power book, Cheshire Books.
- [12] Charrier, B., Constans, J., Cousteau, J.-Y., Daif, A., Malavard, L., & Quinio, J.-L. (1985) Fondation Cousteau and windship propulsion 1980-1985: the Cousteau-Pechiney system *Proceedings of the International Symposium on Windship Technology, Windtech '85*, Southampton, UK.
- [13] McCormick, B.W. (1979) Aerodynamics, aeronautics, and flight mechanics. Wiley.
- [14] Englar, R.J. (1975) Circulation control for high lift and drag generation on STOL aircraft. J. Aircraft 12, 457-463.
- [15] Englar, R.J. (1979) STOL The potential of the circulation control wing concept. *Naval Engineers Journal*, **91**, 99-107.
- [16] Modi, V.J. (1997) Moving surface boundary-layer control: a review. *Journal of Fluids and Structures* 11, 627-663.
- [17] Steele, B.N., & Harding, M.H. (1970) The application of rotating cylinders to ship maneuvering. National Physical Laboratory (Britain) Ship Report 148, Dec. 1970.
- [18] Modi, V.J., Fernando, M., & Yokomizo, T. (1990) Drag reduction of bluff bodies through moving surface boundary layer control. *AIAA Paper 90-0298*.
- [19] Goldstein, S. (1948) Low-drag and suction airfoils. Journal of the Aeronautical Sciences 15 (4), 189-214.
- [20] Brooks, J.D. (1963) The effect of a rotating cylinder at the leading and trailing edges of a hydrofoil. U.S. Naval Ordinance Test Station, *NAVWEPS Rept.* 8042, China Lake, CA, April 1963.
- [21] Tennant, J.S. (1973) A subsonic diffuser with moving walls for boundary-layer control. AIAA J., 11, 240-242.
- [22] Schlichting, H. (1978) Boundary-Layer Theory, Seventh Edition. McGraw-Hill.
- [23] Favre, A. (1938) Contribution à l'étude expérimentale des mouvements hydrodynamiques à deux dimensions. Thesis, University of Paris.

- [24] Favre, A. (1934) Un Nouveau Procede Hypersustentateur: L'aile à Parol d'Extrados Mobile. *Méchanique Expérimentale Des Fluids*, Comptes Rendus, p. 634.
- [25] Truckenbrodt, E. (1952) Die laminare Reibungsschicht an einer teilweise mitbewegten längsangeströmten ebenen Platte. *Abh. Braunschweig. Wiss. Ges.* **4**, 181-195.
- [26] Tennant, J.S., & Yang, T. (1973) Turbulent boundary-layer flow from stationary to moving surfaces AIAA J. 11, 1156-1160.
- [27] Bechert, D.W., Hage, W., & Brusek, M. (1996) Drag reduction with the slip wall AIAA J. 34, 1072-1074.
- [28] Choi, B., & Choi, H. (2000) Drag reduction with a sliding wall in flow over a circular cylinder AIAA J. 38, 715-717.
- [29] Panton, R.L. (1995) Incompressible Flow, Second Edition. Wiley.
- [30] Sirignano, W.A. (1999) Fluid dynamics and transport of droplets and sprays, Cambridge University Press.
- [31] Gad-el-Hak, M. (2001a) Flow control: passive, active, and reactive flow management. Cambridge University Press.
- [32] Jung, W.J., Mangiavacchi, N, & Akhavan, R. (1992) Suppression of turbulence in wall-bounded flows by high-frequency spanwise oscillations *Phys. Fluids A* **4**, 1605-1607.
- [33] Sendstad, O., & Moin, P. (1992) The near-wall mechanics of three-dimensional turbulent boundary layers. Stanford U. Thesis, FPC report TF-57.
- [34] Laadhari, F., Skadaji, L., & Morel, R. (1994) Turbulence reduction in a boundary layer by local spanwise oscillating surface *Phys. Fluids A* **6**, 3218-3220.
- [35] Choi, K.-S., DeBisschop, J.-R., & Clayton, B.R. (1998) Turbulent boundary-layer control by means of spanwise-wall oscillation *AIAA J.* **36**, 1157-1163.
- [36] Keefe, L.R. (1995) Drag reduction by nonlinear flow control. NASA CR-195058.
- [37] Balogh, A., Liu, W.-J., & Krstic, M. (2001) Stability enhancement by boundary control in 2D channel flow *IEEE Trans. Aut. Control*, to appear.
- [38] Aamo, O.M., Krstic, M., & Bewley, T.R. (2001) Control of mixing by boundary feedback in 2D channel flow. Submitted to the *Automatica*.
- [39] Uzkan, T., & Reynolds, W.C. (1967) A shear-free turbulent boundary layer. J. Fluid Mech. 28, 803-821.
- [40] Thomas, N.H., & Hancock, P.E. (1977) Grid turbulence near a moving wall. J. Fluid Mech. 82, 481-496.
- [41] Aronson, D., Johansson, A.V., Löfdahl, L. (1997) Shear-free turbulence near a wall J. Fluid Mech. 338, 363-385.
- [42] Katz J. (1995) Race-Car Aerodynamics Robert Bentley Inc.
- [43] Gad-el-Hak, M., ed. (2001b) The MEMS Handbook. CRC Press.
- [44] Bewley, T.R. (2001) Flow control: new challenges for a new Renaissance. *Progress in Aerospace Sciences* 37, 21-58.
- [45] Orszag, S.A. (1971) Accurate solution of the Orr-Sommerfeld stability equation J. Fluid Mech. 50, 689-703.
- [46] Schmid, P., & Henningson, D. (2001) Stability and transition in shear flows. Springer.
- [47] Potter, M.C. (1966) Stability of plane Couette-Poiseuille flow J. Fluid Mech. 24, 609-619.
- [48] Romanov, V.A. (1973) Stability of plane-parallel Couette flow Functional Analysis and its Applications 7 (2), 137-146.
- [49] Gharib, M. (1987) Response of the cavity shear layer oscillations to external forcing. AIAA J. 25, 43-47.
- [50] Rowley, C.W., Colonius, T., and Basu, A.J. (2002) On self-sustained oscillations in two-dimensional compressible flow over rectangular cavities. *J. Fluid Mech.* **455**, 315-346.

- [51] Koenig, K. & Roshko, A. (1985) An experimental study of geometrical effects on the drag and flow field of two bluff bodies separated by a gap. *J. Fluid Mech.* **156**, 167.
- [52] Gharib, M., & Roshko, A. (1987) The effect of flow oscillations on cavity drag. J. Fluid Mech. 177, 501-530.
- [53] Clauser, F.H. (1956) The turbulent boundary layer, in *Advances in Applied Mechanics*, edited by H.L. Dryden and T. von Kármán, vol. LV, Academic Press, p. 40.
- [54] Tennant, J.S., Johnson, W.S., & Keaton, D.D. (1978) Boundary-layer flows from fixed to moving surfaces including gap effects. *J. Hydronautics* **12**, 81-84.
- [55] Jordinson, R. (1970) Spectrum of eigenvalues of the Orr-Sommerfeld equation for Blasius flow. *Phys. Fluids* **14**, 2535.
- [56] Hocking, L.M. (1975) Nonlinear stability of the asymptotic suction profile *Quart. Appl. Math.* 28, 341-353.
- [57] Gellert, W., Küstner, H., Hellwich, M., & Kästner, H. (1975) *The VNR Consise Encyclopedia of Mathematics*. Van Nostrand Reinhold Co.
- [58] Ashley, S. (2001) Warp drive underwater Scientific American, 284, (5) 70-79.
- [59] Tennant, J.S., Johnson, W.S., & Krothapalli, A. (1976) Rotating cylinder for circulation control on an airfoil. *J. Hydronautics* **10**, 102-105.
- [60] Modi, V.J., *et al.* (1981) Moving-surface boundary-layer control for aircraft operation at high incidence. *J. Aircraft* **18**, 963-968.
- [61] Hendriks, E., ter Heegde, P., & van Prooijen, T. (1988) Aspects of a metal pushing V-belt for automotive cut application *SAE Technical Paper Series* 881734, pp. 4.1311-4.1321.
- [62] Lachmann, G.V. (1961) Boundary layer and flow control: its principles and application, Volume 1. Pergamon Press.

Bio sketch



Thomas Bewley is an Assistant Professor in the Dynamic Systems and Control group of the Mechanical and Aerospace Engineering Department at UC San Diego. He received a B.S. and M.S. from Caltech in 1989, a diploma from the von Karman Institute for Fluid Dynamics in 1990, and a Ph.D. from Stanford in 1998. He and his dog, Morty, direct the Flow Control Lab at UC San Diego. Together with the graduate students and post-docs working in his lab, he is currently investigating a range model-based techniques for the control, forecasting, and optimization of both transitional and turbulent flow systems. Details concerning the current research interests at his lab may be found at: http://turbulence.ucsd.edu